RESEARCH ARTICLE | OCTOBER 07 2024

Characterizing firebrands and their kinematics during lofting

Special Collection: Flow and Climate

Alec J. Petersen ✉ ; Tirtha Banerjee

Physics of Fluids 36, 106611 (2024)
https://doi.org/10.1063/5.0227024

Physics of Fluids ARTICLE pubs.aip.org/aip/pof

Characterizing firebrands and their kinematics during lofting

Cite as: Phys. Fluids **36**, 106611 (2024); doi: 10.1063/5.0227024
Submitted: 5 July 2024 · Accepted: 2 September 2024 ·
Published Online: 7 October 2024

Alec J. Petersen[a] and Tirtha Banerjee

AFFILIATIONS

Department of Civil and Environmental Engineering, University of California, Irvine, 4130 Engineering Gateway, Irvine, 92697 California, USA

Note: This paper is part of the Special Topic, Flow and Climate.
[a]Author to whom correspondence should be addressed: alecjp@uci.edu

ABSTRACT

Spot fires pose a major risk and add to the already complex physics, which makes fire spread so hard to predict, especially in the wildland urban interface. Firebrands can not only cross fuel breaks and thwart other suppression efforts but also directly damage infrastructure and block evacuation routes. Transport models and computational fluid dynamics tools often make simplifications when predicting spot fire risk, but there is a relative lack of experimental data to validate such parameterizations. To this end, we present a field experiment performed at the University of California Berkeley Blodgett Research Forest in California where we recorded the flame and firebrands emanating from a nighttime hand-drawn pile fire using high-frequency imaging. We used image-processing to characterize the fire intensity and turbulence as well as particle tracking velocimetry to measure ejected firebrand kinematics as they are lofted by the plume. We further collected embers that settled around the fire at varying distances and measured their size, shape, density, and settling distributions. We also examine existing physics-based time-averaged models of firebrand lofting and note discrepancies between such models, often used due to their speed and simplicity, and our experimental observations. Finally, we discuss some implications our observations could have on future modeling efforts by considering the time-dependent fire dynamics, intermittency in the plume turbulence, and in the firebrand generation rate. To the best of our knowledge, these are the first *in situ* observations of firebrand generation and lofting from representative fuels, addressing a major source of data gap and uncertainty in the wildland fire literature.

I. INTRODUCTION

Spot fires occur when burning debris is transported by wind over distances ranging from meters to kilometers,[1] but retains enough thermal energy to ignite fuels where they land. This makes containing wildfires challenging as firebrands can cross roads, forest clearings, and fuel breaks made by firefighters to help control the spread. Not only do they complicate firefighting efforts, but they also play a significant role in damaging structures and dwellings in the wildland urban interface (WUI) area.[2–6] Accurately predicting firebrand lofting height is crucial to determining their final settling distance and requires accounting for the coupling between the firebrands themselves, e.g., their size, shape, density, generation rate, their thermodynamics, and their interactions with both the turbulent fire plume and atmospheric turbulence. Most models of the lofting process in particular are often built upon the work of Albini,[7] who derived transport equations assuming a steady buoyant plume to predict properties like maximum spotting distance. These rely on the time-averaged plume representations and ignore turbulence intensity, which can be four to five times greater than the background atmospheric turbulence during fire front passage.[8–11] Still, time-averaged plume models[7,12,13] have been built into many operational models like BEHAVEPLUS[14,15] and FARSITE.[16]

Other models, including more expensive fire behavior tools like WFDS that use large-eddy simulations (LES) to solve for time-dependent numerical solutions for the governing equations for mass, momentum, and energy, frequently use other simplifying assumptions. These range from using spherical[7,17–21] or regular disk or cylindrical[7,13,19,22,23] or a combination of both[24,25] to represent firebrand shapes, ignoring the thermodynamics of firebrands as they travel[22] or assuming constant settling velocities,[17,26,27] known to be inaccurate for particles settling in turbulence.[28,29] Parameterizations of the complex coupled physics[30–33] can decrease computational cost, yet they often have limited experimental verification, making it difficult to assess which factors may impart inaccuracies in the model predictions.

There are few experimental studies of firebrand dynamics in the field due to the myriad complications that arise from safety concerns and associated technical challenges. Recently, Bouvet *et al.*[34] reported on an experiment tracking firebrands downstream of a firebrand generator that aimed to identify the firebrand combustion state, and with capabilities to identify firebrand shape and size. However, as far as we are aware, our study is unique for its characterization of firebrand generation and kinematics of a fire representing the burning of actual wildland fuels *in situ*.

Laboratory studies have investigated mass and size variations in embers generated from burning conifer trees or similar fuels.[35–42] Firebrand transport has also been investigated in laboratory settings.[43,44] Some of the few experimental studies done *in situ* during prescribed burns described the nearby firebrand flux as well as the fire rate of spread, though did not report on the firebrand kinematics.[45,46]

This work aims to fill some of those experimental gaps and weave together firebrand lofting kinematics as well as the size, shape, and density of firebrands lofted by a fire burning a mixture of fuels, as is the case in wildland fires. To that end, we report on a field experiment of a pile fire where we both track firebrand trajectories as they are ejected from the fire and collect ember samples to statistically describe their size, shape, and density characteristics. Pile burns are a type of prescribed burns where instead of "broadcasting" a fire on a landscape, surface fuels and masticated fuels are collected in heaps and ignited. This is a safe way to reduce fuel loads that would have added to surface fuel loading exacerbating wildfire risk. We take advantage of such a pile fire since it offers a safe way of characterizing the burning of the same wildland fuels, since it is not spreading. More generally, however, it is virtually impossible to fully characterize the fuels feeding a wildland fire. By using a mix of fuels from the local environment (as detailed in the methods, roughly a 75/25 mix between ponderosa pine and Douglas-fir, with the 1-h fuels having a moisture content of 9%), including pine needles, branches, and lumber from cut down and fallen trees, our pile included the various materials that would fuel a wildfire in this biome. Past laboratory experiments have studied the burning characteristics and embers from carefully characterized fuels;[40,47] however, that information is often missing for natural wildland fires and not available as inputs for modeling. Moreover, such detailed studies must focus on a select number of fuel species,[40] for example, focuses on fine fuels: the ends of branches with their leaves from Douglas fir, Eucalyptus globulus, and Coast live oak trees. Our pile was instead made up of the full size range of fuels resulting from mechanical treatment of the surrounding forest. By burning this wide range of fuel types, our experiment aims to characterize the embers and their lofting in an uncontrolled field setting more representative of the conditions found in wildland fires. We further use the flame height evolution to describe the fire intensity and turbulence of the flame and discuss the intermittency of the flame vs that of the firebrand generation. The fire evolution is also important to the firebrands' velocities and accelerations, and we show how the coupling between the plume and the firebrands changes as the turbulence evolves along with the fire. We end by examining some time-averaged, physics-based models of firebrand lofting and discrepancies between the models, often used due to their speed and simplicity, and our experimental observations that could help inform future modeling efforts.

II. METHODS

A. General set-up

We performed our experiment at the University of California (UC) Berkeley Blodgett Research Forest, a mixed conifer forest in the foothills of the Sierra Nevada Mountains in California. We constructed the pile from a thinning of small trees, approximately a 75/25 mix between ponderosa pine (*Pinus ponderosa*) and Douglas-fir (*Pseudotsuga menziesii*). The fuel was a mixture of fine and coarse woody fuels. Fine fuels included 0.6–8 cm diameter pieces but also pine cones and needles. We also included larger 12–18 cm diameter fuels in the piles. We used a GoPro Hero Black 9 to record full HD (1920 × 1080 pixel) mp4 movies at 119.8 Hz, which allowed us to capture the time-resolved flame and firebrand dynamics during the burn. We recorded the first 18 min of the pile fire, capturing the flame evolution through ignition, peak flame, and initial decay for a total of ~130 000 images. A schematic of the experimental setup is shown in Fig. 1(c), along with some of the relevant scales, namely, $D = 1.6$ m, the initial pile diameter, and L_f, the flame height. The pile was built to a height of 2 m. To achieve the largest field-of-view (FOV) while still resolving individual firebrands, we placed the camera at a 4.13-m standoff distance from the pile center and tilted it at 27.5° from the horizontal to capture a region of interest (ROI) from 0.5 to 6.2 m above ground level, with 1.2 m of horizontal distance on each side.

To calibrate our measurements, we must take into account the tilt angle of the camera, which changes the distance between the lens and the FOV at different heights. The object distance (L_O) for rows in the upper portion of each image is larger than for the rows at the camera height, causing non-uniformity in the magnification and thus the pixel resolution. Following Ref. 48, we use the GoPro's linear view focal length (16.5 mm) and the object distance for the central row in the image frame in the thin lens equation ($1/f = 1/L_O + 1/L_i$) to calculate the corresponding image distance from the lens (L_i). This allows us to calculate the camera magnification and pixel resolution at the central image row, as 3.4 mm per pixel. This initial estimate is used to calculate the object distance along the rows of the image, which is then input into a second iteration of the calibration to correct the magnifications at different heights using $M(i) = L_i(i)/L_O(i)$, where $M(i)$, $L_i(i)$, and $L_O(i)$ are the magnification, image distance, and object distance at each pixel row, *i*. The non-uniform pixel resolutions at different elevations caused by the camera tilt range from 3 to 5.4 mm pixel^{-1}. These maps of the non-uniform pixel resolutions allow us to calculate displacement maps for each pixel, which we input into MATLAB's geometric image transformation function, *imwarp*, to correct the perspective with the FOV center as the anchored reference point such that each pixel has a uniform pixel resolution. We confirm the pixel resolution and FOV extent using the pre-burn pile height, which we measured separately during the setup. The uncertainty for the pixel resolution is dependent on the angular measurement device accuracy (0.1°) and the camera standoff distance from the pile center, which we estimate to be 10 cm. This leaves us with an uncertainty of 2.1% for the pixel resolution, which corresponds to a maximum uncertainty of 0.03 mm pixel^{-1}. An example image frame after magnification correction is shown in Fig. 1(a), with arrows representing firebrands tracked in the current frame and colored according to their velocity magnitude. Figure 1(b) instead shows pathlines indicating a sample set of firebrand trajectories again colored by their velocity magnitude.

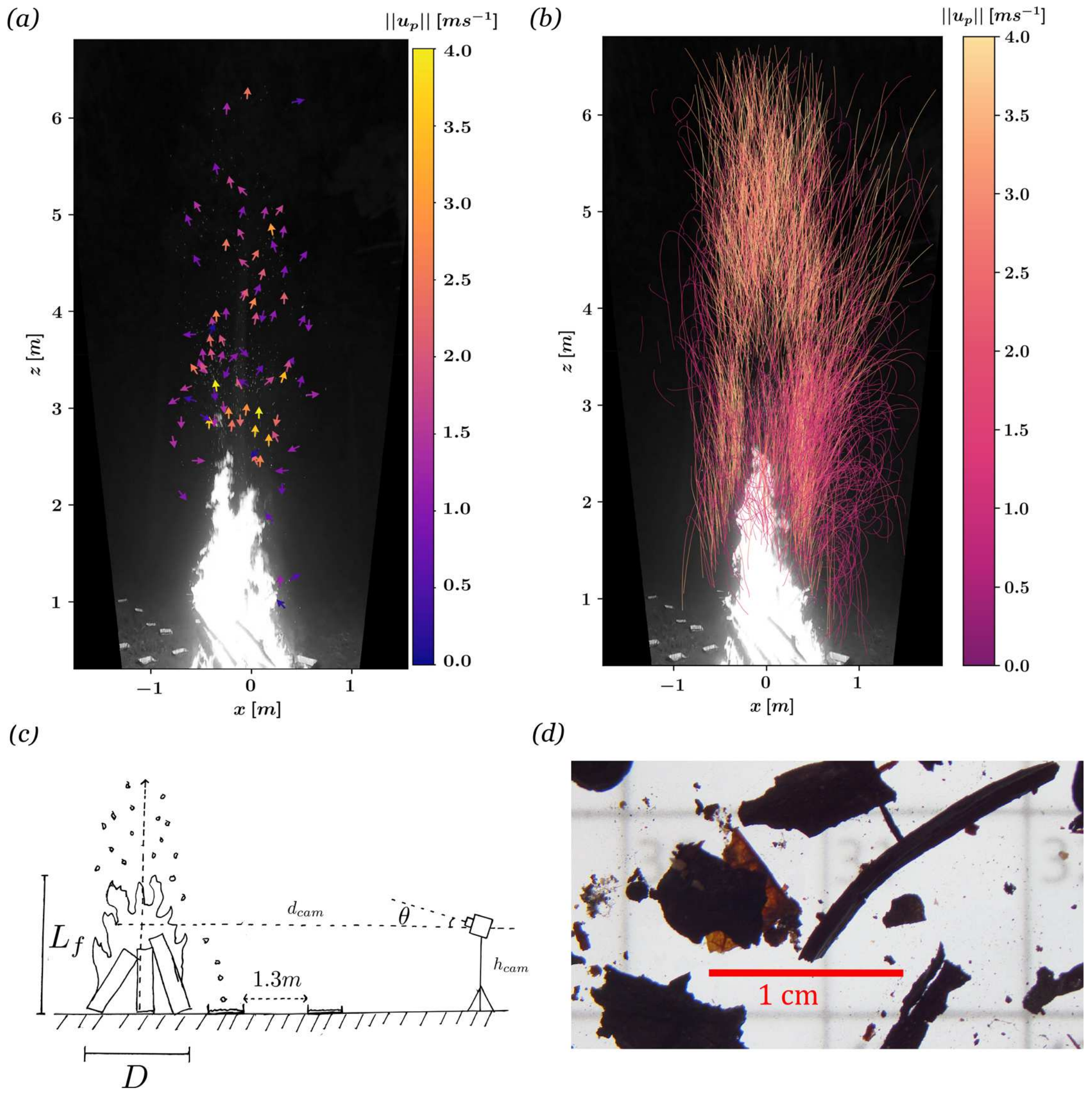

FIG. 1. (a) Example frame from the video recordings after perspective warping, with arrows indicating firebrands tracked in the frame and colored by the measured velocity magnitude. (b) Firebrand pathlines for a subset of trajectories. Aluminum ember collection trays can be seen in the lower left. (c) Representative schematic of the experimental set-up. (d) Example of embers imaged under a microscope for shape and size characterization.

Environmental wind was minimal during the course of the experiment. Using the contours of the flame extracted from the videos, the flame tilt was calculated using the moments of the contour to calculate the orientation of the major axis of the bounding ellipse, which we show in Fig. 2(a). The flame was found to predominantly tilted straight upward, with a slight bias to the right and a standard deviation of 16°. For all practical purposes, we can, therefore, assume that fire was not strongly influenced by the ambient wind, but rather dominated by the buoyant fire plume itself. To confirm this assumption, we monitored wind speeds at the Blodgett Forest meteorological tower and show the mean and maximum measured wind speeds over the course of the experiment in Fig. 2(b). These measurements were taken at a 3 m height and peaked at $0.4\,\mathrm{ms}^{-1}$, but averaged closer to $0.2\,\mathrm{ms}^{-1}$ providing support that ambient wind played a minimal role over the course of the experiment.

B. Image processing

After the magnification correction, the images were preprocessed using minimum intensity background subtraction and then thresholded by a pixel intensity that we found by visual inspection best isolated the brightest features of the images, including the flame and the firebrands. The largest contiguous contour after thresholding was labeled as the flame and then masked out in each frame of the recording so we could track only the firebrands. We used those flame masks to calculate the flame height evolution. The masked and background subtracted images were then fed into a particle tracking velocimetry

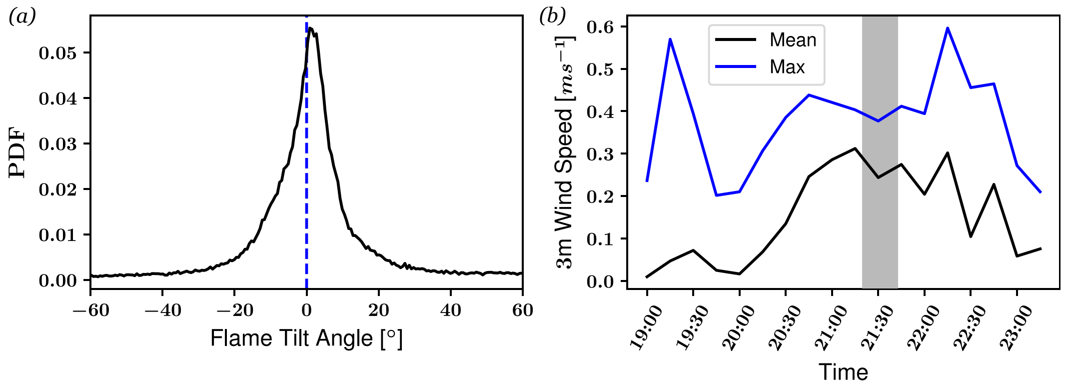

FIG. 2. (a) PDF of the flame tilt angles. (b) Time series of mean and maximum wind velocities measured at the local Blodgett meteorological tower at a height of 10 m. Gray shaded region represents the duration of the experiment.

(PTV) algorithm. The algorithm we use is an in-house version of the fourth-frame best estimate as described in Ouellette *et al.*[49] The first step is particle segmentation to identify individual firebrands, which we do following a method similar to that of Khalitov and Longmire.[50] We set all pixels below a threshold intensity to zero, which we choose based on visual inspection of the images. Contiguous groups of non-zero pixels are identified and labeled and then filtered by size. Groups of pixels larger than 50 pixels in area are discarded as these correspond to flickering portions of the flame, disconnected from the rest of the flame body. Appendix A includes a more detailed accounting of our particle-finding process.

The particle-segmentation algorithm has its own limitations and is reliant on the thresholding chosen as well as the concentration of particles. For example, during the peak flame phase, we observe many concentrated bursts of firebrands, and if the particles appear too close to one another in the image, particle segmentation will be unable to distinguish the particles and label them as one. Thus, we may be underestimating the firebrand count, especially during these concentrated bursts. We calculate the particle centroids from their sub-pixel center-of-mass, which then are fed into the tracking algorithm to connect their trajectories between frames. Afterward, their velocities are accelerations are determined by convolving their positions with the first and second derivatives of a Gaussian kernel, respectively. The width of the kernel is chosen following the procedure established for tracer particles in G. A. Voth *et al.*,[51] and applied to inertial particles in Refs. 52–55. This convolution is necessary to reduce the random noise associated with firebrand position uncertainty and to prevent it from contaminating the Langrangian statistics. Figure 5(a) shows the probability density function (PDF) for the final firebrand trajectory lengths after processing.

C. Ember collection and characterization

We also collected embers in $11'' \times 9''$ aluminum baking trays filled with water to douse the embers upon settling around the pile. Six ember collection trays were placed radially every ~15° from 166° SW to 265° SW (the direction of the forecast ambient wind) at 1.3 m separations and single trays were placed around the rest of the fire 1.3 m from the pile edge at the spacing of ~30°. Unfortunately, wind direction changed between setting up and waiting for nightfall, leading to only a single ray of trays collecting significant numbers of embers. At the end of the experiment, we collected and labeled the samples of water and embers and brought them back to the lab for analysis. The collected mixture of water, ash, and embers was first mixed to homogenize it and subsequently five 10-ml samples were poured from each tray into test tubes. We diluted these five subsamples by factors of 5, 10, or 50-to-1 by volume depending on their particle density such that particles would appear distinct under the microscope. Each subsample was then filtered to remove the water, and the remaining embers were placed onto separate slides such that all present particles could be imaged and sized. We chose the number of subsamples to balance the constraints of time and statistical convergence. For the most dilute trays, these five subsamples still provided us with $O(1000)$ embers to characterize and ensure that we captured a representative sample of the largest embers. A lower number of samples risked biasing our data, since these rare large embers were not necessarily present in any single subsample, despite comprising a considerable percentage of the total collected mass in each tray. After imaging each subsample under the microscope, we used threshold-based image segmentation and edge-detection to calculate ember size and shape as discussed in Sec. III A, which includes statistics from over 86 000 individual particles. Finally, to determine the mean ember density, we utilized an automatic gas displacement pycnometer (Micromeritics AccuPyc II) at the UC Irvine Materials Research Institute. After imaging, we took a 20 g (approximately 10% by mass) sample of the embers previously imaged, to estimate the bulk ember density. We used the pycnometer to measure the volume of three separate portions of the ember sample, again chosen due to time requirements for the process. We then weighed them with a microgram-precision scale (Mettler-Toldeo GmbH MS105DU, 0.001 mg sensitivity). We arrived at a mean ember density of $360 \pm 9\,\mathrm{kg\ m^{-3}}$, with the uncertainty here accounting for both the measurement error and the standard deviation of the three subsamples to estimate the sampling error.

III. RESULTS

Our experimental observations are organized as follows: in Sec. III A, we examine the characteristics of embers that settled into our collection trays including their size and shape. In Sec. III B, we discuss the evolution of the fire itself using the flame height to estimate the heat release rate (Q). We also investigate the relationship between the flame intensity and the firebrand generation rate. Finally, in Sec. III C, we use the results of our PTV algorithm to investigate firebrand velocity and acceleration statistics, including spatial maps of the firebrand mean velocity and their variance as well as firebrand ejection angles.

A. Ember characterization

1. Ember density

We are able to calculate a bulk density for the embers that we collect during pile burn by taking a representative subsample of our embers and using a pycnometer (MicroMeritics AccuPyc II) to measure the volume of the material contained within the sample and a scale (Mettler-Toldeo GmbH MS105DU, sensitivity of 0.001 mg) to measure its mass. Ponderosa pine and Douglas fir have dry wood densities of 350–450[56,57] and 530–560 kg m^{-3},[58] respectively. These are both denser than our measured bulk ember density of 360 ± 5 kg m^{-3}, which we expect due to the embers undergoing thermal degradation. Transport models are sensitive to firebrand density, and such a reduction will have a significant impact on their settling rate. However, some studies use the unburnt-fuel density in their transport calculations,[59] which may lead to unrealistic results. On the other side of the spectrum, the simulations of Ref. 21 varied firebrand density from 50 to 150 kg m^{-3} and investigated their landing densities. Such low values may not be representative of what one would observe in a forest fire, which typically burns fuels like wood and bark with higher densities. As Woycheese[60] noted, low-density wood species typically burn to completion while higher-density species self-extinguish with considerable leftover material, making the 50%–90% reduction an overestimation of the reduced density of firebrands compared to their fuels. Firebrands from industrial materials, such as roof shingles, will have their own characteristics, which also need to be considered. Unfortunately, there is no single firebrand density that can be used realistically for any given situation. The matter is further complicated by the reality that firebrand density is not static but in fact changes with time as the firebrand smolders, which makes incorporating a combustion model essential if the physics are to be realistically modeled, something very few simulations have done in the past.

2. Ember concentration

As described in Sec. II, we image samples of embers from collection trays placed around the pile fire under a microscope to characterize ember concentration, shape, and size in two dimensions. Figure 3(a) shows the relative concentration of embers in each tray as a function of distance. The concentration of embers in each sample

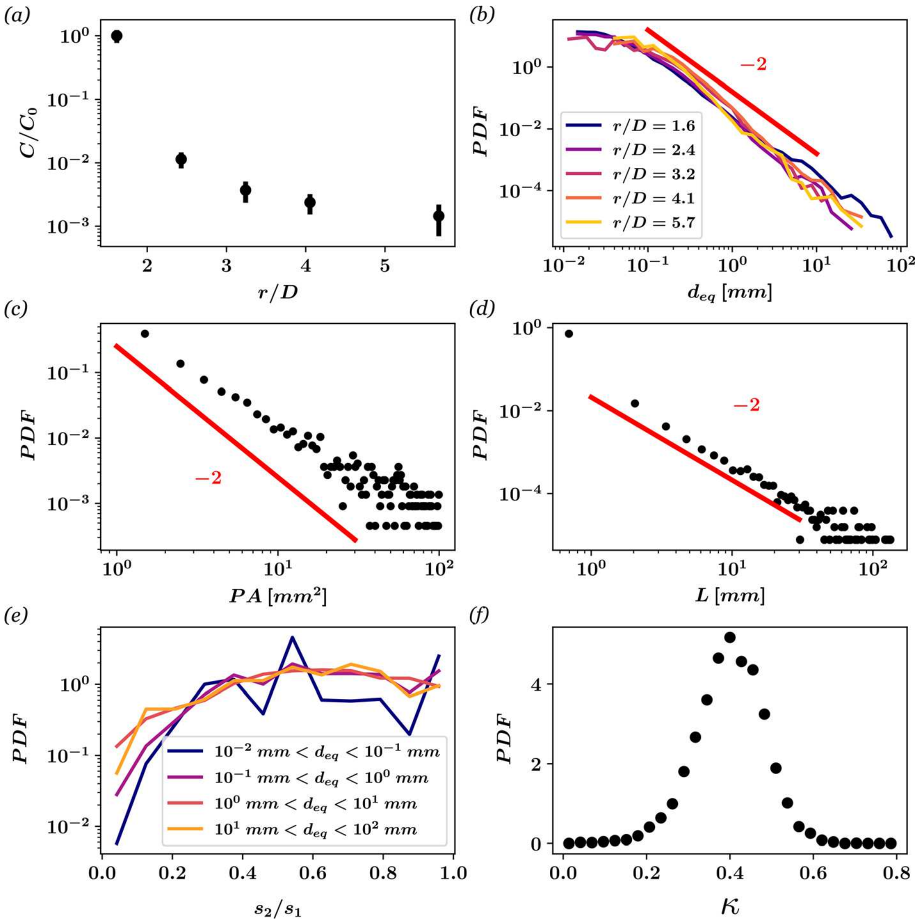

FIG. 3. (a) Concentration (relative to that of the closest collection tray, C_0) as a function of radial distance normalized by the initial pile diameter. (b) PDFs of ember equivalent diameter from downwind collection trays at increasing distances from the fire. (c) PDF of ember projected area as seen in images. Red line indicates a power law with a slope of -2. (d) PDF of the longest dimension of each ember, again with the -2 power law plotted in red. (e) PDF of the aspect ratios, s_2/s_1, i.e., the ratio of the shorter dimension to the longer dimension, for the collected embers. (f) PDF of the ember shape complexity, κ for the collected embers.

decays exponentially with distance similar to findings by Sardoy *et al.*,[13] Wang,[61] Thurston *et al.*,[62] and Martin and Hillen.[63] These embers come from the five collection trays downwind of the fire where we observed the most accumulation. We are able to identify approximately 86 000 individual embers in our images ranging from microscopic ash particles a few pixels in our images to embers over 10 cm in length (3d). Our method of sampling embers is unique in this regard compared to previous studies either in the laboratory[35,36,64] or in the field,[38,39,45,65] where usually, individual embers are picked out to be characterized. As described in our Sec. II, because we image diluted and homogenized water samples containing embers, we are not biasing our ember characterization by pre-selecting, which embers to analyze. Instead, we are only limited by the resolution of the microscope imaging system, allowing us to describe a much larger range of ember sizes.

3. Ember size

Figure 3(b) shows PDFs of the particle equivalent diameter (equal to the diameter of a circle with equivalent area, $d_{equiv} = \sqrt{4A/\pi}$) for particles from the five closest collection trays, which span almost three decades from 100 μm to 10 cm. Unsurprisingly, the largest embers with diameters greater than 1 cm are more likely to be found closer to the fire. Their early settling is also partially responsible for the exponential decrease in ember concentration described previously. While the smaller particles may be embers, aggregate soot, or ash, which may not contribute to spotting, their presence here reveals an interesting scaling, not noted in previous experiments characterizing embers. Figures 3(c) and 3(d) show PDFs of the projected area and length of the sampled particles and display the same scaling as in Fig. 3(b), which all seem to follow power laws with slopes near -2. These differ from observations of the past,[37,66] which most often report lognormal distributions for ember area and length. Because our imaging method allows us to resolve such a wide range of particle sizes, we are not size selecting before analysis in the way past studies have[65,67] and instead are characterizing all particulate matter our microscope camera can resolve, from microscopic ash to those larger partially burned pine needles and bark fragments. Such predetermination of relevant particles to size could determine the previously reported size distribution shape, rather than representing the reality of how fires generate particulate matter. The observed self-similarity will be present no matter where one defines the relevant size to be considered a firebrand with spotting risk and moreover it is significant since it implies that ember breakage and generation may not occur with a characteristic or mean size in the context of mixed wildland fuels.

Interestingly, this is the same scaling as shown in Ref. 69 for dust particle size distributions in the atmosphere. They determined that the -2 scaling behavior is a direct consequence of the fragmentation process itself. As Ref. 68 explains, the scale invariance in the fragmentation of the brittle material (in our case, wood) is due to the propagation and merger of cracks. These cracks then locally weaken the material, leading to further fragmentation or even total failure, where pieces of fuel fall upon each other, introducing even more fragmentation through impact. Our observation of the same power-law behavior suggests a similar fragmentation process is responsible for generating embers in our pile and could inform ember generation models that incorporate polydispersity. As a consequence of the power-law behavior of said distributions, we do not observe ember size distributions with a defined mean or mode, which could be important in simulations where ember size probability distributions (if not assuming a single ember size for simplicity) need to be input. Practically, simulations need to limit the size range, since resources are limited and, as noted, microscopic ash particles would not be relevant for investigations of firebrand spotting. Instead, the size range included in the spotting predictions should focus only on embers that could practically ignite nearby fuels after landing, which will depend on ember size, material, and wind/turbulence conditions. However, these observations could still be used to inform ember size distributions used in simulations of spotting from wildland fires without imposing a distribution informed from a biased measurement method.

4. Ember shape

We also characterize the shapes of embers imaged under the microscope. Figure 3(e) shows the PDF of the ember aspect ratios, s_2/s_1, where a value equal to one indicates a shape equal in length and width like a circle, and values approaching zero indicate a highly elongated object. Although a few elongated embers appear in our samples, like pine needle fragments, the vast majority are less extreme. In fact, there is a relatively wide range of aspect ratios, from $0.3 < s_2/s_1 < 1$, that we find in equal proportion. We also characterize ember shape through a measure called the complexity of a two-dimensional (2D) shape,[69] which combines three criteria to describe a shape contour: (i) entropy of the global distance distribution (GDD), (ii) entropy of the local angle distribution (LAD), and (iii) shape randomness. Following Ref. 69, the GDD is the distribution of distances of all points in the shape outline to its centroid while the LAD measures the contour's local smoothness and regularity and includes a measure of the perceptual smoothness of the contour. Shape randomness is quantified using the distance between different traces through the contour point set using a standard nearest-neighbor-based trace searching algorithm.[69] Chen and Sundaram describe their weights for these factors in the complexity measure κ, which we follow. The values of κ close to 0 indicate a simple shape such as a circle, and values larger than 0.6 indicate high complexity such as a near-random cloud of points.

Figure 3(f) shows a PDF of the measured complexity values for the largest 1000 ember samples, which have the most complex contours (made up of hundreds or thousands of pixels rather than just a few for the small particles). These embers display a mean complexity of ~0.37, with a standard deviation of 0.08. One way to interpret this level of mid-to-low complexity would be to imagine a polygon with added noise to the contour. Computational studies of ember transport often assume simple shapes for the firebrands, using volumetrically equivalent spherical counterparts to approximate a range of particle shapes. However, these assumptions can dramatically affect long-range transport.[70] Although we were unable to characterize the 3D shape of the collected embers, the depth of the largest imaged embers was at least qualitatively smaller than the length or width, indicating that disk shapes are a decent simplification. At the same time, our results do quantitatively show that incorporating some randomness to the polygonal disk shapes to make them non-equilateral would be more representative of embers observed in a fire composed of mixed-fuels: here in a pile fire or in an actual wildland fire where a similar mix of fuel types and sizes would all be present in an overgrown forest plot.

B. Flame evolution

1. Flame height and heat release rate

Figure 4(a) plots the time evolution of the flame height of the pile fire, L_f, extracted from the recorded video. The lighter line represents the raw time series, while the dashed dark red represents the heat release rate, Q, estimated from the low-pass filtered flame height following Heskestad[71] as

$$Q = \frac{32(51D + 50L_f)^{5/2}}{2209\sqrt{47}} \quad [W], \tag{1}$$

where $D = 1.6$ m is the fire diameter.

While acknowledging that the Heksestad correlation is not an exact measure of the heat release rate, it provides an approximate estimate, allowing us to compare, at least qualitatively to other fire configurations. The estimated heat release rate of the pile fire peaks around 4 min into the experiment at just over 2900 kW and then decays to 800 kW at the end of our recording. Although it is difficult to assess the uncertainty of this estimate, we have reason to believe that it is within a reasonable factor of the true heat release rate,[72] precisely measured Q by placing Douglas fir trees on a scale and measuring the mass lost as the tree burned. For a 2 m tree (the closest of their samples to our pile height of 1.5 m), they found their average $Q_{\max} = 5200$ kW. Although this is nearly our maximum value, we note that their experiment took place over a single minute before the tree was completely burnt, whereas our pile burned much more slowly—our recordings last 18 min, but the fuel took over an hour until it was spent. Our pile had considerably more mass than any of the single trees[72] tested, leading to that longer burn time. Over the course of the recording, we also noticed that the flame seems to have distinct phases with different dynamics. Initially, during the first 2 minutes of the burn, the flame height grows rapidly, followed by the next 2 minutes where the flame height reaches and sustains a peak height before beginning to decay. This first decay phase is not quite as rapid as the growth phase, but over the course of 4 minutes, it decays in height by almost half. The last phase is the slow decay, which lasts for the remainder of the recording and during which the flame continues its decay, but at a slower rate losing 40% of its initial height over the course of 10 minutes. These phases are represented in Fig. 4(a) by the shaded regions. These flame phases will have significant impacts on the firebrand dynamics, as described later.

2. Firebrand generation characteristics

We also count the number of firebrands present in each video frame, which we plot as a time series in Fig. 4(b). This time series bears a resemblance to the flame height series, at least when low-pass filtered, though there are notable differences, e.g., the delayed peak in the firebrand count, N_e, when compared to the flame height. We should note, however, that firebrand count is only an indirect measure of their generation and is dependent on our particle-segmentation algorithm, which has its own limitations. For example, when the firebrands are quite concentrated and appear side-by-side in the images, the algorithm will struggle to distinguish between the two and count them as a single particle. During the peak flame phase, we observe many concentrated bursts of firebrands and thus may be underestimating their count during these periods.

The fluctuating components of flame height, L_f', and firebrand count, N_e', are plotted together in Fig. 4(c) for comparison. Low coherence between the fluctuating signals hints that there are different stochastic processes in this pile fire underlying the flame height and firebrand generation. Indeed, the power spectral density of the flame height fluctuations plotted in the top inset in Fig. 4(c) displays a clear $-5/3$ slope, indicative of the expected Obukhov–Corrsin scaling for passive scalar fluctuations in turbulence.[73,74] However, the turbulence inside the fire does not appear to be responsible for the firebrand generation fluctuations. Indeed, the power spectrum density of the firebrand count shows an entirely different scaling behavior. We see further evidence for the separation between the turbulent plume dynamics and the fluctuating firebrand count when we look at the probability densities of these quantities.

While the flame height fluctuations have a large variance during the growth and peak phases that increase up to the peak flame height around 4 min, the firebrand count variance is remarkably consistent throughout the same period. Close to the 5-min mark, at the beginning of the initial flame decay phase, the firebrand count suddenly becomes highly intermittent, with large bursts, orders of magnitude larger than previous fluctuations. The PDF of the flame height fluctuations [Fig. 4(d)] is close to a normal distribution, whereas the firebrand count fluctuations [Fig. 4(e)] are highly intermittent with an extreme kurtosis, $\kappa = 60.5$. Such a large kurtosis is not characteristic of turbulent velocity fluctuations in fire plumes or atmospheric surface layer flows, which can range from around 3 to 10.[75,76] In fact, as noted in Sec. II, the environmental wind was negligible for our purposes, and the flow was dominated by the turbulent buoyant fire plume. We see this both in the measurements from the meteorological tower, and also from the flame tilt angle statistics shown in Fig. 2(a) in Sec. II. We assume that the flame tilt is a representative measurement of the background wind turbulence, which is made more plausible as they share similar values of kurtosis ($\kappa_{\text{tilt}} = 6.68$) to those measured in atmospheric flows. This bolsters our confidence that any background turbulence from the wind is minimal as the flame is rarely more than 10° in either direction, indicating that the flow is instead dominated by the buoyant fire plume.

We further compare PDFs of the zero-crossing times for both fluctuating signals [Figs. 4(f) and 4(g)]. Here we again observe the extreme intermittency in the firebrand count signal. While the flame height fluctuations have a steep drop off in probability for zero-crossing times greater than 3 s, the firebrand count displays consistent self-similarity in the probability up to multi-second periods without zero-crossings. Interestingly, we also see similarities to other studies of intermittency, namely, Chowdhuri *et al.*,[77] who looked at persistence probability density functions for velocity and temperature fluctuations in the surface layer of a turbulent convective boundary layer. For the flame height fluctuations in particular, we see the same power-law behavior with an exponent of -1.6[77] and found the cutoff for this power-law behavior in the persistence PDFs to occur at the integral time scales. While we do not have a direct measure of the integral time scales for the vertical plume velocity fluctuations, we use the autocorrelation of the fluctuating flame height signal to calculate a timescale where the autocorrelation function decays to zero. We do the same for the firebrand count fluctuations and plot them as the vertical dashed lines in Figures 4(f) and 4(g). The associated timescale for the flame height fluctuations is a sort of proxy for the turbulent integral timescale since the flame structure is determined in large part by the air turbulence. This autocorrelation timescale further lines up precisely with the cutoff of the power-law behavior in the flame height fluctuation zero-crossing PDF, recalling the observations of Chowdhuri *et al.*[77]

The firebrand count fluctuation zero-cross PDF in Fig. 4(g) does suggest a similar power-law behavior, though there is not as clear a relationship between its associated autocorrelation timescale and a change in the behavior of the zero-crossing PDF. This difference in the intermittency and the behavior of the zero-crossing PDFs between the firebrand count and flame height signals suggests that there is not a simple correlation between the fire (and associated buoyant plume turbulence) and the firebrand generation process. Since neither atmospheric wind nor the plume are plausible generators of such intermittency, the fuel bed itself, whether through structure collapse or another mode of weakening and fracturing is the likely candidate as discussed when examining the ember size PDF and fracturing hypothesis.[68] The various failure modes for wood that could lead to ember generation are discussed by Caton-Kerr *et al.*,[78] who studied thermal degradation of wooden dowels. Burning materials undergo thermo-mechanical instabilities, pyrolysis, and oxidation, which introduce micro-cracks and fractures. While these thermal degradation processes alone can cause failure and generate embers, the presence of external loadings (e.g., through wind drag), temperature gradients, or other constraints is often more significant. Whether the fracturing modes they identify lead to a similar power-law size scaling seen here and in Kok[68] would be an interesting future direction for research. One aspect of ember generation not discussed in Caton-Kerr *et al.*,[78] is mechanical breaking due to collapse, a mechanism, which from visual observation, was significant in our pile fire. In both controlled and uncontrolled wildland fires, where overgrown vegetation can collapse onto each other this mechanism could be responsible for a large proportion of firebrand generation, and would not be captured in generation models that do not consider the spatial organization of fuels.

3. Comparisons between flame and firebrand generation characteristics

For modeling purposes, it would be convenient if there was a consistent relationship between the fire intensity and the firebrand generation that would lend itself to simple parameterization. Despite the qualitative similarity between the signals, the fluctuating components in particular show little correlation. Still, most parameterizations of firebrand generation often rely on some measure of fire intensity as the controlling parameter. For example, in the PHOENIX RapidFire, McCarthy *et al.*[79] use the convective strength of the fire to determine the proportion of firebrands lofted. Wickramasinghe *et al.*[25] similarly

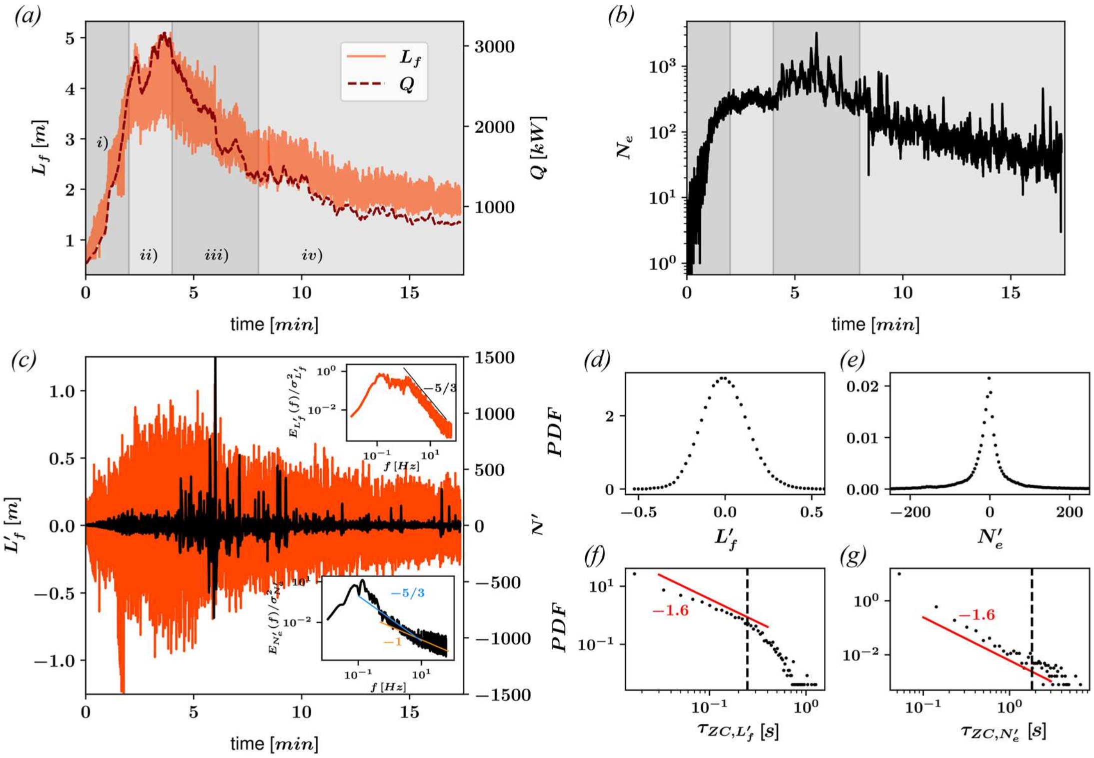

FIG. 4. (a) Time series of the flame height, extracted from recorded video and the heat release rate of the pile fire, Q, estimated from the low-pass filtered flame height measurement, following Heskestad,1984.[71] The shaded regions indicate our subdivision of the fire into distinct phases: (i) flame growth, (ii) peak flame, (iii) initial (fast) flame decay, and finally (iv) the longer and slower decay. (b) Time series of the firebrand count in the experimental field-of-view over the course of the 18-min recording. (c) The fluctuating components of both the flame height and firebrand count, with insets showing the spectral density for both. (d) and (e) The PDFs for the flame height fluctuations and the firebrand count fluctuations, respectively, with the former following a nearly Gaussian distribution with a kurtosis $\kappa = 3.15$, vs the extreme kurtosis for the firebrand count fluctuations where $\kappa = 60.5$ (f) The PDF of the zero-crossing times for flame height fluctuations and (g) the same but for the firebrand count fluctuations.

tie the firebrand injection rate in their simulations to the heat release rate of the fire.

While such parameterizations may capture the coarse-grain behavior of the firebrand generation, they ignore the high intermittency in the firebrand count signal. Those bursts make a significant contribution to the number of firebrands released over the lifetime of our experiment and do not follow a simple pattern, i.e., as the fire dies down, the firebrand count signal is still significantly intermittent, whereas the flame height fluctuations steadily decrease. Furthermore, as discussed previously, the process of firebrand generation is dependent on the material properties of the fuels themselves: how they crack and fragment. This is different than assumptions used in some models of firebrand generation, like that of Ju *et al.*,[40] where firebrand yield is a function of the drag applied by the buoyant plume onto the burning fuels. The importance of those bursts and the material properties of the fragmentation process, therefore, may need to be incorporated into future models for firebrand generation, which could be sampled from a highly intermittent PDF as in our experiment.

One limitation of the current study is that we cannot investigate the relationship between firebrand generation and environmental wind speed, which Bahrani[37] showed to be an important controlling parameter. It is possible, for example, that in larger-scale fires, or fires subject to more extreme wind conditions, that breakage from drag out competes the combustion-related mechanisms we seem to be observing here: fracturing due to structure collapse, cavitation, and general fuel degradation. Further work is necessary to quantify the intermittency of firebrand generation in such fires. However, even if mechanisms like drag breakage play a large role under those circumstances, the fracturing and collapse mechanisms present here will still lead to a highly intermittent signal, which should be addressed in simulations.

C. Firebrand kinematics

We calculate the firebrand kinematics for over 400 000 individual trajectories, though the majority of these are tracked for a limited duration as seen in Fig. 5(a), which shows the probability distribution for the trajectory lengths in seconds. Most trajectories are quite short, due to a few factors. Firebrands rapidly cool and cease emitting visible light for our camera to observe. The PTV algorithm can also lose track of firebrands if they move too far out of plane, too fast, or if due to high firebrand concentration, it becomes too difficult for the algorithm to match particles between frames. We are able to follow firebrand trajectories for a maximum of 2 s (240 consecutive frames), though the mean trajectory lasts only about 0.4 s, corresponding to about 48 consecutive image frames. We detail the PTV uncertainty in Appendix A, and in Appendix B, we estimate the lower size bound for tracked firebrands during the PTV analysis, which is of $O(1)$ mm in diameter due to both the camera resolution and the expected time before firebrands stop emitting visible light.

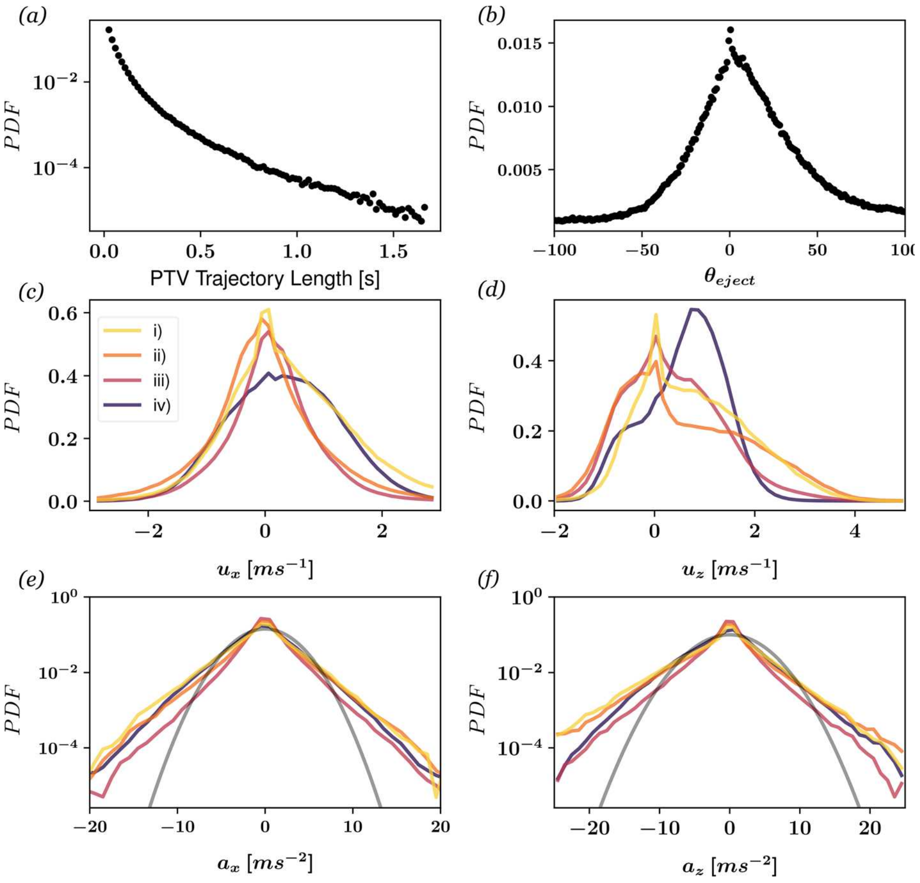

FIG. 5. (a) PDF of the trajectory durations measured from PTV. (b) PDF of the ejection angles of firebrands. PDFs of firebrand (c) horizontal and (d) vertical velocity separated by fire phases (i) flame growth, (ii) fire peak, (iii) flame initial decay, and (iv) slow flame decay. The same separation is replicated in (e) and (f), which show PDFs of the firebrand horizontal and vertical acceleration, respectively.

1. Firebrand ejection angle

We first examine the ejection angles as defined by the initial velocity vector our PTV algorithm calculates for each trajectory. The ejection angle, θ_{eject}, is defined relative to the z-axis, with positive angles pointing toward the $+x$-axis and negative angles toward the $-x$-axis. The PDF of θ_{eject}, shown in Fig. 5(b), has a primary peak at $\theta = 0°$, corresponding to purely upward movement. However, we observe a widespread of ejection angles, with the distribution displaying a standard deviation of 33°.

2. Firebrand velocity

Figure 5 shows the PDFs for horizontal (c) and vertical (d) firebrand velocity in our experimental domain, a roughly 2.5 m by 6.5 m box centered on the pile. The PDFs have been split by the phase of the fire in which each firebrand resides to highlight the time evolution of the statistics. There is a slight positive skew to the horizontal velocities, due to the slight background wind (as detailed in Sec. II). We observe more interesting physics in panel (b), where the vertical velocity distributions change drastically over the course of the experiment. During the flame growth and peak flame phases, we observe distributions with means only slightly greater than zero, but with long skewed-positive tails. Finding a firebrand with a vertical velocity of $2\,\mathrm{ms}^{-1}$ is more than five times more likely in these periods than in the later flame-decay phases.

Interestingly, as the flame dies down, the mode of the vertical velocity distribution shifts to large positive (upward) values. This evolution seems to follow the evolution of the buoyant plume: as the fire is developing, the plume is highly intermittent—indicated by the large variance in the flame height. Later, it develops a consistently strong plume that can sustain large mean buoyant forces but is less intermittent with fewer strong turbulent bursts. Common to each of these PDFs is their multi-modal nature, representing that firebrands are not purely ejected upward, but also fallout from the edges of the plume and are occasionally re-entrained into the plume to potentially be lofted once again.

3. Firebrand acceleration

Figures 5(e) and 5(f) similarly display PDFs of the horizontal and vertical acceleration statistics, separated by fire phase. Both sets of PDFs have long tails when compared to a normal Gaussian distribution, shown by the gray line, characteristic of the coupling between the intermittency of turbulence in the plume and the inertia of the firebrands.[51,80] The vertical acceleration has a kurtosis of 6.75, which varies over the fire phases. Kurtosis over the first phase ($\kappa_{a_z,i} = 5.91$) is initially lower, which increases during the fire peak and initial decay ($\kappa_{a_z,ii} = 7.35$ and $\kappa_{a_z,iii} = 8.46$, respectively) before decaying with $\kappa_{a_z,iv} = 4.95$. The horizontal acceleration follows a similar pattern. Additionally, we observe the same division between the growth and decay phases in the vertical acceleration, where firebrands in the first phases are more likely to experience extreme acceleration.

The narrowing of the acceleration PDFs with fire phase is reminiscent of the effect of Stokes number (*St*), the ratio of a particle aerodynamic timescale to one of the turbulent flow, on acceleration statistics. Increasing *St*, and thus particle inertia, results in narrowing distributions of acceleration, since the increasingly inertial particles are more resistant to the rapid accelerations of small-scale turbulence (filtering the high-frequency fluctuations of the fluid acceleration) as seen both experimentally[55] and in computational work.[81,82] One way to interpret the trend in the vertical acceleration PDFs is that firebrand inertia increases (i.e., the effective *St* increases) relative to the turbulent motions of the buoyant plume as the fire develops. Assuming that the shape and size of the firebrands generated do not change during the fire development, we can thus infer that the turbulence itself is particularly intense during the flame growth and peak phases, leading to the long tails of the vertical firebrand velocity.

4. Buoyant plume structure

Although in the present study we cannot directly observe the buoyant plume, we can visualize some of its structure by looking at spatial maps of the firebrand velocity as in Fig. 6. Figures 6(a)–6(d) show the mean vertical velocity as a function of the firebrand positions from the center of the plume normalized by the initial diameter of the pile, x/D, and the vertical distance normalized by the height of the instantaneous flame, z/L_f. During the flame growth and peak phases, the plume is strong and has limited horizontal spread. There is a clear boundary where the mean vertical velocity is zero, represented by white in the figure. Inside the core region, the plume is, on average, strong enough to loft firebrands, while outside, it is weaker and firebrands are more likely to start settling. This boundary widens as the fire evolves and enters the decay phases, supporting our earlier argument regarding the more consistent upward buoyant force firebrands are subjected to over a larger area as the fire begins decaying. We can also see this in Figs. 6(e)–6(h) where the variance of the firebrand vertical velocity is relatively large throughout the fire plume, especially when compared to the decay phases. Firebrands ejected during the peak phase, while experiencing large turbulent fluctuations and strong buoyant forces, also have to contend with possibly being ejected out of the strong updrafts of the plume if their ejection angles are skewed slightly off-axis. These firebrands will then start to settle, contributing to the lower mean of the velocity distribution during this phase and the larger downward fluctuations in the acceleration PDF.

IV. DISCUSSION

A. Implications for modeling

Simplifications are of course necessary when predicting a phenomenon as complex as firebrand transport and spotting. Even the most detailed large-eddy simulations used to model firebrand lofting and transport filter the smallest scales and parameterize their effect on the firebrands to reduce computational cost. We discuss some common simplifications and assumptions in Sec. IV A 1, including (i) determining lofting height using time-averaged fire plume models; (ii) ignoring plume turbulence and inertial effects; (iii) ember shape simplifications; and (iv) firebrand release rate parameterizations. The following discussion demonstrates that each simplification makes sense in the context of mean firebrand transport behavior; however, if predicting spot fire risk is the goal, the risk from low probability events needs to be accounted for. Over the billions of firebrands released during a wildland fire event, it is likely that many large firebrands will be ejected during strong bursts of upward acceleration, helping transport them far distances with enough leftover thermal energy to ignite spot fires. Determining which parameterizations filter out such statistically

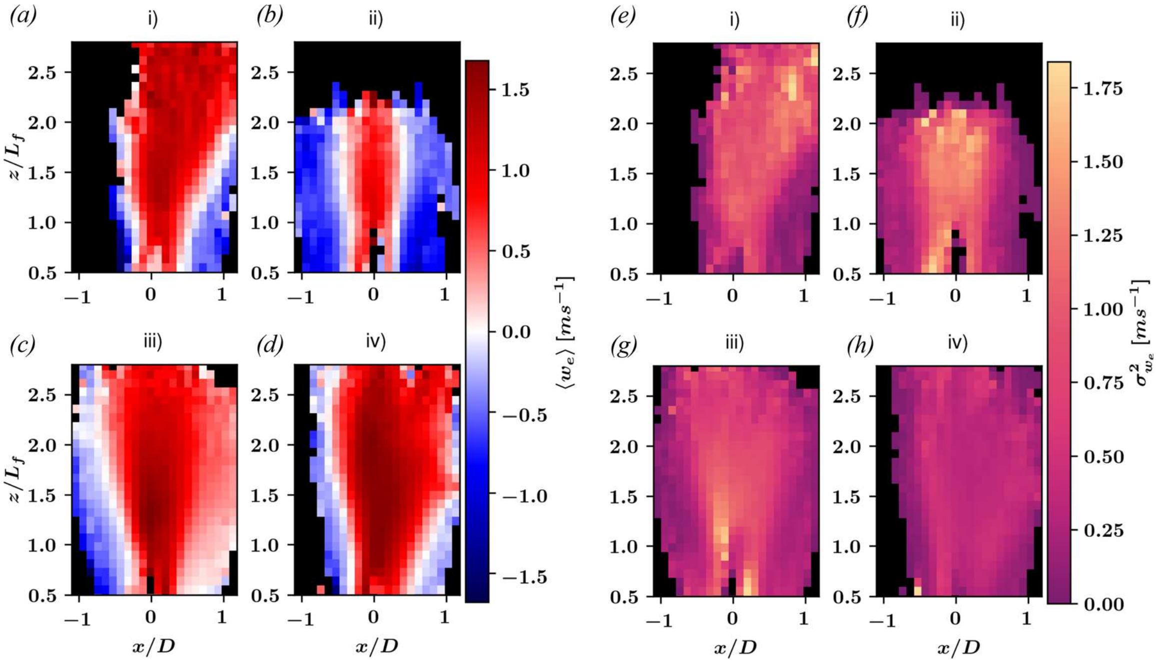

FIG. 6. (a–d) Eulerian-mean velocity fields of firebrands with the horizontal dimension normalized by the initial pile diameter and the height, z, normalized by the flame height and separated by fire phases (i)–(iv). (e–h) Variance of the velocity fields with the same normalization and separation.

rare occurrences and what new parameterizations need to be developed to account for such events is key to better spot fire prediction.

1. Firebrand lofting height

Larger firebrands, which we categorize as larger than 10 mm in equivalent diameter, are most relevant for igniting spot fires, since they can combust or smolder long enough to land far from the source. Many of the simpler physics-based models, like those of Himoto and Tanaka[22] and Woycheese *et al.*,[18,19] estimate lofting height based on the Baum and Mccaffrey[83] model or another similar time-averaged fire plume model. While Woycheese *et al.*[19] extended their original model to account for disk-shaped embers, often these models assume spherical embers for simplicity in calculating drag coefficients and thus the forces felt by firebrands within the buoyant plume, an assumption that even more complex LES also make.[24,31,84,85] As noted by Wadhwani *et al.*,[1] the in-built drag models of FDS include only drag formulations for cylindrical or spherical particles. Such simplifications can be useful especially when trying to quickly predict where spot fires might occur, but those assumptions can also lead them to underestimate the risk firebrands may pose. For example, Woycheese *et al.*[18] modeled fires using the aforementioned Baum and Mccaffrey[83] model and a simple force balance for the firebrands taking into account drag and gravity. These equations can be rearranged to solve for the maximum brand size a fire of a given intensity (quantified by its heat release rate) can loft as: $d_{max} = 2\langle\frac{\rho_f}{\rho_p}\rangle\langle\frac{Q}{\rho_f c_p T_0 \sqrt{g}}\rangle^{2/5}$, where ρ_f and ρ_p are the fluid and particle density, respectively, Q is the heat release rate, c_p is the specific heat of the fuel, T_0 is the ambient temperature, and g is gravitational acceleration.

In Fig. 7(a), we present the maximum predicted height (z_{max}) from models based on the time-averaged Baum and Mccaffrey[83] plume equations for various firebrand sizes, assuming sphericity and three estimated fire intensities from the pile burn corresponding to the peak, growth, and decay phases. While millimeter-sized firebrands can be lofted nearly 100 m, z_{max} drops precipitously with increasing particle size. Using our peak heat release rate of $Q = 2900$ kW, these models can only loft firebrands smaller than 10 mm in diameter. At smaller heat release rates, this maximum loftable firebrand size decreases: 7.6 mm at 1500 kW and 6 mm at 800 kW. Given that we collected embers >10 mm over 9 m away from our pile, this prediction is an underestimation of the fire's potential to loft the large firebrands, the very ones with enough thermal energy to ignite spot fires. While the heat release rate we estimate from the Heskestad correlation may only be an approximation of the true value, the qualitative results stand even if our estimate is off by a factor 2. Steady-state plume models are unable to produce the forces necessary to loft and transport the large, >10 mm embers, which we observe many meters from the fire.

The firebrand lofting height is a critical predictor of final spotting distance since the injection height into the atmospheric boundary layer will determine what cross-wind speeds the firebrands will experience. Yet, as we have shown, lofting models built using time-averaged fire plume equations for vertical air velocity have significant shortcomings. The relatively low-power pile fire in the current experiment was able to loft firebrands up to nearly $d_p = 100$ mm at least 9 m from the pile, where our collection trays ended. These particle sizes (assuming sphericity) could not be lofted away from the fire at all if the air velocity was modeled with the Baum and Mccaffrey,[83] or another similar time-averaged plume model.[18,19] It should also be kept in mind that these models also present a best-case scenario: assuming firebrands are

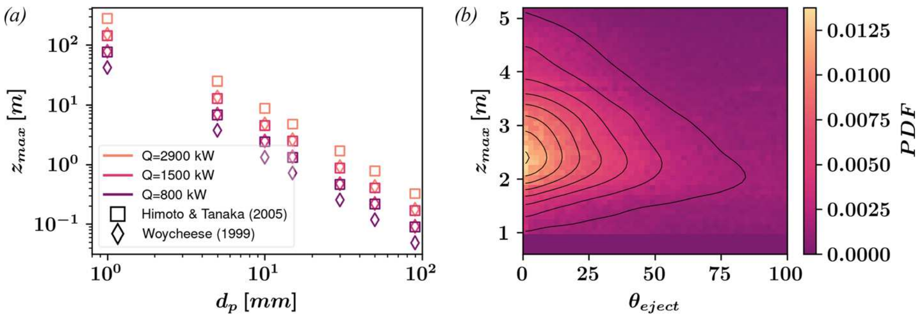

FIG. 7. (a) Maximum lofting heights (z_{max}) according to the models of Woycheese *et al.*[19] and Himoto and Tanaka[22] for fire heat release rates (Q), from different moments of our pile burn experiment. (b) Joint PDF of firebrand ejection angles and maximum trajectory height, $z_{e,max}$.

experiencing the largest vertical velocities at the centerline of the plume. However, in practice, firebrands are dispersed throughout the plume and will thus encounter significantly small mean vertical velocities. Yet, in our experiments, even firebrands ejected off-axis have significant probabilities of being lofted to the top of our camera's field of view.

While Fig. 6(b) showcased the large variance of ejection angles centered around $\theta_{eject} = 0$, Fig. 7(b) is a joint PDF between the ejection angle, θ_{eject}, and maximum observed height of firebrand trajectory, $z_{e,max}$. Firebrands ejected vertically are most likely to be lofted to the limits of our camera's field-of-view, as expected. Still, we observe many firebrands ejected at skewed angles, or ejected outside of the fire centerline and thus according to the Baum–McCaffrey model, should experience relatively weak updrafts. Figure 6(b) reveals, however, that many of these firebrands are still frequently lofted to considerable heights. For example, firebrands ejected at a skewed angled of 25° are only 66% less likely to be lofted to 4.5 m than firebrands ejected completely vertically. Often, the firebrands leave our field of view or are lost by the tracking algorithm at these heights with significant vertical velocities, suggesting the possibility they have not yet reached their apex.

2. Effects of shape and size on firebrand lofting

As discussed in Sec. II A, we quantify the ember shape by examining their aspect ratios and a shape complexity value. The majority of embers were mildly elongated and the contours of the largest 1000 ember samples had a moderate complexity level, indicative of polygonal shapes with added noise. These measurements suggest that modeling firebrands as regular polygonal shapes like ellipses and hexagonal disks is a plausible simplification. We do not, however, find a clear "average ember" shape; aspect ratios have some size-dependency, but range from values of 0.3 to 1 with relatively equal probabilities. Using a single ember shape in simulations may thus miss out on important physics.

On the other hand, some ember shapes may be more interesting from a transport perspective. Past work[24] showed that the disks in particular, with their large drag coefficients when oriented with their largest projected area normal to the flow direction, can be transported over distances many multiples that of similarly sized spheres. This could justify limiting the shapes and sizes of firebrands in simulations, if for example, examining long-range transport was the focus of the study. However, from laboratory studies of disks falling through turbulent flows,[86] we also know that depending on the flow and particle parameters, such objects could also oscillate or tumble, complicating calculations for their drag coefficient. Without fully resolving the flow around such disk-like firebrands, the drag coefficient has to be parameterized itself, all of which will impact the final predicted settling distance. As Thomas *et al.*[46] noted in their analysis of embers collected at different distances from a prescribed burn: "…while the number of particles may show an inverse relationship with distance, there is no such trend with the particle projected area. This highlights the complexity of the deposition process…." Additionally, more disk-like firebrands could experience significant aerodynamic lift forces, complicating the particle equation of motion used in simulations. Indeed with such complex, coupled physics involved in firebrand settling, it is difficult to draw any but the most broad conclusions about how firebrand shape will affect final deposition distance. However, future simulations may benefit from including multiple shapes, perhaps informed from the statistics presented in this study.

3. Implications of plume turbulence and inertial effects

In addition to evidence from the collection trays, we also see the influence of the plume turbulence reflected in the velocity and acceleration distributions, where the evolving nature of the fire plume has significant effects on the intermittency of large firebrand vertical velocities and accelerations. Including turbulence parameterizations through LES,[87] or by using the turbulent kinetic energy solved for by FIRETEC[90] to drive firebrand motions could capture some of these effects. Capturing intermittent effects in the lofting model will be important for predicting the rare events where large firebrands, those potentially most dangerous for igniting spot fires, reach high heights, and thus can be transported long distances. With the enormous volume of firebrands emitted from even a small fire, such relatively rare events may be significant in the spotting process. Computational studies, such as Thurston *et al.*,[62] have shown that turbulent plume dynamics are indeed important, increasing the maximum spotting distance and the lateral spread by up to a factor of two compared to their LES without plume turbulence.

Our field observations do agree with the general conclusion that realistic spotting distances cannot be predicted without taking into account the plume turbulence. We also note that the firebrand–turbulence coupling throughout the atmospheric boundary layer could be important to consider. With some assumptions about typical atmospheric conditions, e.g., a Kolmogorov microscale ∼0.25 mm, the larger firebrands in our study will have significant Stokes numbers, St_η, of order 0.1 (corresponding to firebrands with $d_p \approx 5$ mm), where inertial effects become important for phenomena like clustering, and enhanced/attenuated settling speed.[29] Especially in simulations where the subgrid physics are parameterized, it may be important to keep such coupled physics in mind. Enhanced settling could, for example, increase the fall speed of larger firebrands once they leave the influence of the plume by a factor of 2 or 3, not only decreasing the airborne time but also increasing the probability that these large firebrands will retain enough thermal energy to ignite fuels where they land.

4. Implications of firebrand generation mechanism and intermittency

Some studies, such as Anthenien *et al.*,[24] assume that the ember separates from its parent material with zero initial velocity and that all acceleration is due to the plume itself. While simplifying the math greatly, there are no experimental studies we are aware of that evaluate the significance of that assumption. Qualitatively, from visual observations, the firebrands are ejected with a wide variety of speeds and angles, seemingly disconnected from the fire plume itself. One avenue of future research should delve deeper into firebrand generation processes and initial ejection velocity—it is possible, for example, that as the fire size increases, that initial ejection velocity becomes insignificant when compared to the plume's buoyant power. Accordingly, this would also suggest a fire size (or buoyancy flux) at which ejection velocity becomes significant for overall transport, but such investigations would require careful laboratory studies.

Finally, as we discussed earlier, while there are some correlations between the heat release rate and firebrand generation, as seen in the present study as well as others;[64,88] such coarse-grained correlations miss out on the extreme intermittency, which could lead to drastic over or under-estimations of the firebrand generation rate as in some simulations.[25] Large bursts of firebrands released intermittently could have a significant effect on the number of firebrands lofted and transported long distances—if a burst of firebrands is released during a particularly strong updraft, a larger proportion of those firebrands will be injected higher up into the atmospheric boundary layer and thus reach further spotting distances. Additionally, the coincidence of an intermittent firebrand burst with an intermittently strong plume updraft would have the effect of lofting a greater proportion of the largest firebrands higher up than current models or simulations predict. Breakage due to drag may be more relevant for higher-intensity fires subject to large forces from large atmospheric wind and plume velocities and so should not be ignored. However, intermittency has not to our knowledge been accounted for in firebrand generation models, which may contribute to discrepancies between simulations and observed spot fire behavior.

V. CONCLUSION

This study presented a unique field experiment in which firebrands were tracked as they were ejected and lofted by a pile fire. Embers were further collected in trays placed around the fire to analyze their size and shape. To our knowledge, this is the first experiment where firebrands are generated from real representative fuels and are characterized *in situ* along with their kinematics.

Over 86 000 embers were imaged under a microscope to evaluate their two-dimensional size, described by the equivalent diameter, projected area, and the maximum length of the collected embers. Unlike previous studies where embers are manually collected and imaged, our method for diluting and imagining ember samples does not suffer from the same selection biases present in those studies. We find that their density is lower than unburnt fuel density, but not as low as many models assume, which can range from 10% to 50% of the unburnt values. The ember sizes vary quite widely over four orders of magnitude and the size distributions follow a power law with a -2 scaling. Although ember concentration decays exponentially from the source, we observe large ($>$10 mm) diameter particles at our furthest collection point, 9 m away. We further quantify the ember shape by examining their aspect ratios, and a shape complexity value. The majority of embers were mildly elongated and the contours of the largest 1000 ember samples had a moderate complexity level, indicative of polygonal shapes with added noise. However, further analysis of the three-dimensional firebrand shapes is needed to evaluate whether such regular shapes are good approximations for the variety of irregular ember shapes that exist in nature.

Using simple thresholding on our images, we are able to extract information about the flame evolution itself through the fluctuating flame height. We use this measurement to estimate the fire heat release rate, throughout our 18-min experiment. We also examine the relationship between the flame height and the firebrand count per frame, which acts as a proxy for the firebrand generation rate. Although the firebrand count increases with flame height, and thus fire intensity, the two are not well correlated and seem to be driven by different processes. While the flame height fluctuations do indeed follow the expected Obukhov–Corrsin scaling in its spectra, the firebrand count is much more intermittent and follows a different scaling. We see further evidence for the extreme intermittency of the firebrand count fluctuations by looking both at the kurtosis of its probability density function as well as the long tail of its zero-crossing PDF. This intermittency has not to our knowledge been accounted for in firebrand generation models, which generally are formulated with a simpler, direct relationship between the heat release rate and the number of firebrands released per unit time. Large bursts of firebrands released intermittently could have a significant effect on the number of firebrands lofted and transported long distances—if a burst of firebrands is released during a particularly strong updraft, a larger proportion of those firebrands will be injected higher up into the atmospheric boundary layer and thus reach further spotting distances. Additionally, the coincidence of an intermittent firebrand burst with an intermittently strong plume updraft would have the effect of lofting a greater proportion of the largest firebrands higher up than current models or simulations predict. Such an effect could be responsible for the large embers we observe transported at least 9 m from the pile fire, and future studies could simultaneously measure the air-phase and firebrand kinematics to analyze this mechanism.

Measurements from PTV on the firebrands allow us to characterize their ejection angles from the pile as well as velocity and acceleration statistics during the lofting process. We find that the fire intensity has a significant impact, particularly in the vertical component of the velocity and acceleration. We can infer from the firebrand kinematics that the growth and peak fire phases exhibit considerable turbulence, leading to large variances in those quantities when compared to the decay phases.

We also provide a discussion of the implications these collected observations might have on future modeling efforts. We argue that firebrands observed in our video recordings come from the greater than 1 mm range of embers collected from our settling trays since smaller sizes are both unlikely to be either resolved by our camera and coold own too quickly for our camera's framerate to pick them up before reaching temperatures at which they would cease radiating light in the visible spectrum. We then compare the expected lofting height of firebrands in that larger size range from simplified time-averaged plume models of Woycheese *et al.*[19] and Himoto and Tanaka[22] to our observations. We suggest that such models underestimate the potential for larger firebrands to be lofted and transported considerable distances due to the combination of assumptions made, including spherical particle shapes, forgoing plume turbulence, and that firebrands are released with zero initial velocity, with all their acceleration due to the plume. The last assumption implies particles are ejected purely upward, but our measurements show a wide range of ejection angles, and although firebrands ejected with small angles from the vertical have the highest likelihood of traveling to the limits of our experimental domain, firebrands that are ejected off-axis, and thus experience significantly smaller mean plume velocities, still have relatively high chances to be lofted quite high. We conjecture that intermittent turbulent updrafts are essential to lofting the large firebrands, which are most dangerous for igniting spot fires, and thus it cannot be ignored when trying to predict spotting.

While the present study provides valuable experimental data to be used as validation for different model parameterizing of firebrand lofting processes, there are limitations to the experiment that should be addressed in future studies. The two-dimensional nature of the PTV both increases uncertainty in the velocity and acceleration statistic and a future study that measures these quantities in all three dimensions would provide more accurate and comprehensive kinematic information. With the setup of the present experiment, we were also unable to measure the plume air flow which would help investigate the force experienced by individual firebrands as they traverse the plume. Three-dimensional shape analysis of the collected embers instead of the two-dimensional imaging performed here would also be valuable to determine the drag and lift forces experienced by firebrands. Finally, one of the greatest limitations of this study was our inability to know the size and shapes of the firebrands tracked by PTV in our video recordings. This could be remedied by undergoing a similar experiment but using a camera with much higher resolution so that individual firebrands can be fully resolved and tracked simultaneously, which would allow one to connect the firebrand velocity and acceleration to their size and shape characteristics.

ACKNOWLEDGMENTS

AP and TB are supported by the U.S. National Science Foundation (Nos. NSF-AGS-PDM-2146520, NSF-OISE-2114740, NSF-CPS-2209695, NSF-ECO-CBET-2318718, and NSF-DMS-2335847), the University of California Office of the President (No. UCOP-LFR-20-653572), NASA (No. 80NSSC22K1911), and the United States Department of Agriculture (Nos. NIFA 2021-67022-35908 and USDA-20-CR-11242306-072). The authors report no conflict of interest. The authors thank Professor Adyemi Adeleye and Hugo Yao for helping with microscopic observations of the embers as well as Professor Rob York for all his help and expertise during our field experiments at Blodgett.

AUTHOR DECLARATIONS

Conflict of Interest

The authors have no conflicts to disclose.

Author Contributions

Alec J. Petersen: Conceptualization (equal); Data curation (equal); Formal analysis (lead); Investigation (lead); Methodology (lead); Software (lead); Validation (equal); Visualization (equal); Writing – original draft (lead); Writing – review & editing (equal). **Tirtha Banerjee:** Conceptualization (equal); Data curation (equal); Funding acquisition (lead); Project administration (lead); Resources (lead); Supervision (lead); Writing – original draft (supporting); Writing – review & editing (equal).

DATA AVAILABILITY

The data that support the findings of this study are available from the corresponding author upon request.

APPENDIX A: PTV UNCERTAINTY QUANTIFICATION

Figure 8 illustrates the image processing steps, with zoomed-in example frames to show the firebrands we segment and track with PTV. Due to constraints of resolution and relatively deep depth-of-field we do not use these images to size firebrands since the uncertainty would overwhelm the measurement. Thresholding therefore is most significant for the number of firebrands detected. As displayed in Fig. 8(d), we use the intensity signals from local maxima to estimate an initial threshold (half of the mean particle maximum), which we then refine by visually inspecting the images. In these experiments, that meant raising the threshold slightly to avoid overlapping particles during particularly dense bursts of firebrands, which does ultimately reduce the number of firebrands detected and tracked during PTV as dimmer firebrands are ignored. Although this biases us toward smaller firebrand counts [e.g., in the time-series shown in Fig. 4(b)], we still track over 400 000 individual firebrands. Additionally, the firebrand counts reported in Fig. 4(b) are not meant to be interpreted as the actual total number of firebrands released over the lifetime of the fire, but instead the firebrands bright enough to be captured by our camera, which we assume to be representative of the ember generation rate. We, therefore, accept this trade-off to optimize particle-finding for the bright firebrands and our velocity and acceleration statistics.

Both random uncertainty, due to the finite sample size, and bias uncertainty, due to systematic errors affect the final estimation of the uncertainty of the velocity. Two sources of bias uncertainties come from estimating the particle centroid and the magnification uncertainty as previously discussed. These however are relatively small. The magnification uncertainty is about 2%, and we can estimate the particle centroid uncertainty by testing out the centroid finding method on synthetic particle images with added Gaussian noise. The sub-pixel center of mass method we use is very reliable, correctly identifying the centroids for 1000 synthetic particles with an uncertainty of 0.1 pixels. However, this uncertainty is an order of magnitude smaller than the typical firebrand displacement between frames, and therefore its impact is minimal.

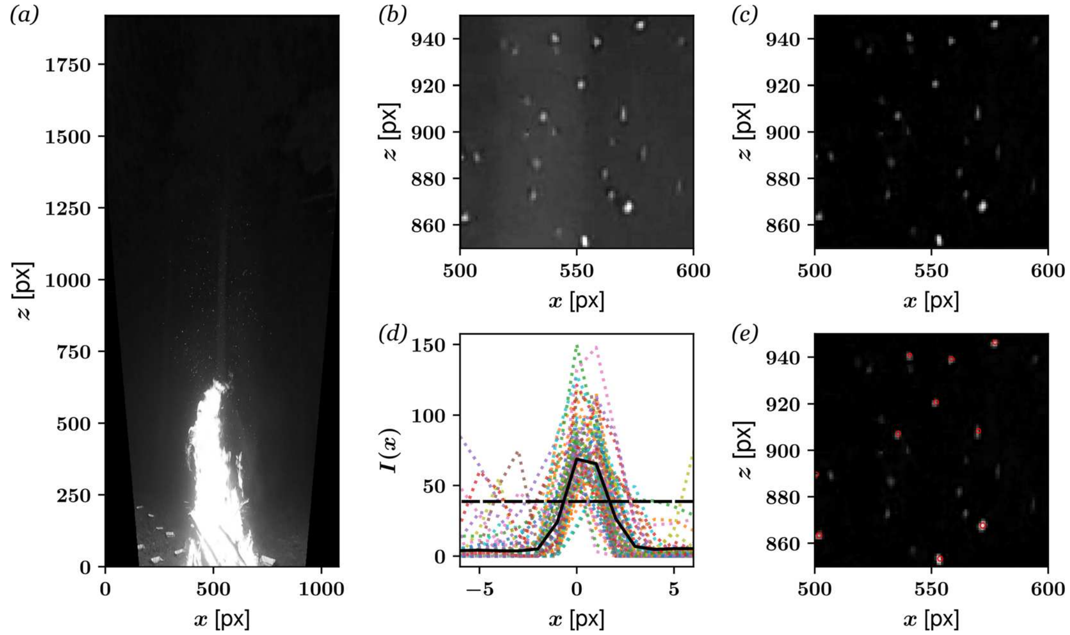

FIG. 8. (a) Perspective-corrected image (b) zoomed-in section before background subtraction and (c) after background subtraction (d) horizontal pixel intensity values [$I(x)$] from individual particles (dotted colored lines) and averaged over all particles (solid black line) along with the final chosen threshold (dashed black line) (e) final tracked particles noted by red circles.

The largest contributor to velocity and acceleration uncertainty comes from our experimental setup. Despite the three-dimensional nature of the flow, our single camera projects the displacement of the firebrands onto a single plane, centered on the pile. Any out-of-plane motion is completely lost, leading to potential underestimation of the actual firebrand velocity magnitude. Fortunately, this uncertainty only applies to the out-of-plane velocity component and does not affect the in-plane displacement, particularly the vertical displacement which is most relevant to our discussion of lofting. However, it is important to note that the actual three-component velocity magnitude could be significantly larger than our results here suggest.

More important is that unlike in laboratory PTV studies where the cameras have relatively shallow depths-of-field, or where a laser sheet illuminates only a sliver of the whole experimental volume, the depth-of-focus for the GoPro goes to effectively infinity and the lack of light sheet illuminating particles implies that we could be tracking firebrands significant distances from the central plane of the fire plume, which we use to calculate our camera magnification and pixel resolution. The further a firebrand from that central plane, the more inaccurate our velocity and acceleration measurements become when converting from pixels/frame to SI units. Since we have no measure of the firebrand out-of-plane location, we can only estimate this uncertainty. Under the assumption that the majority of firebrands will be lofted from within the diameter of the pile ($D = 1.5$ m), we assume that at maximum we are tracking firebrands ±0.75 m from the central plane centered on the fire as shown by the z-axis in Fig. 1(a). This results in a further uncertainty on the pixel resolution of 0.19 mm pixel^{-1}, which adds an additional 15% uncertainty. Propagating the uncertainty for the velocimetry from the three sources: (i) magnification uncertainty due to standoff distance and tilt angle uncertainty, (ii) magnification uncertainty due to the firebrands' potential out-of-plane position, and (iii) centroid-finding uncertainty leaves us with a final systematic bias of 16% for our velocimetry measurements. While large compared to laboratory studies using PTV, we note the challenging conditions of the present field-scale study and that this is the first time to our knowledge that such techniques have been applied to firebrands lofted under a forested canopy. Although some caution should be taken with regard to comparing the velocity and acceleration measurements we have made to other experiments or simulations, the qualitative conclusions of the present work are not expected to be overshadowed by this uncertainty.

APPENDIX B: TRACKED FIREBRAND SIZE ESTIMATION

While the embers we characterized from our collection trays range in size from microscopic to tens of millimeters, those size distributions are not going to be representative of the firebrands we track in our recordings with PTV. Images from the cameras used in this experiment do not contain sufficient detail to resolve firebrand size and shape, and often firebrands we track appear as one or two pixels in the frame. Although that makes it hard to discuss the forces each firebrand is subjected to as we follow it along its trajectory, we can at least put limits on the size range we can resolve and track. Based on camera resolution alone, a single pixel corresponds to approximately 1 mm, depending on where the pixel occurs within the frame. While glowing firebrands could appear bigger than their true size in the camera sensor, it is unlikely that our camera can pick out anything smaller than $O(1)$ mm in diameter.

This $O(1)$ mm diameter lower-limit is further supported by modeling the firebrand temperature rate of change. We estimate the time it takes for a firebrand to cool down sufficiently to stop glowing, assuming blackbody radiation and a glowing temperature of 798 °C, the temperature at which a blackbody stops radiating in the visible spectrum (and thus would be visible to our camera). Once firebrands cease smoldering our camera is unlikely to make them out at night when we record the videos irrespective of their size. We make this estimate by following the work of Anthenien *et al.*[24] and Urban *et al.*,[89] the former being one of few studies to consider the thermodynamics of firebrands into modeling their dynamics and the latter investigating the temperature evolution of firebrands subjected to varying wind speeds in a wind tunnel. Using the assumption of Anthenien *et al.*[24] that the combustion reaction has ended we combine their Eqs. (17)–(19) for the temperature rate change dT_e/dt with Eqs. (2)–(7) from Urban *et al.*[89] resulting in a system of equations that can be solved to determine dT_e/dt as a function of wind speed and firebrand diameter. While the reader is referred to their papers for the full details, the equations are outlined here.

We first numerically solve for the firebrand temperature:

$$Q_{rxn} h_{MT} \rho_{air} YO_2 = h_{HT}(T - T_\infty) + \varepsilon\sigma(T^4 - T_\infty^4), \qquad \text{(B1)}$$

where $Q_{rxn} = 2.51$ MJ/kg is the energy released from the oxidation reaction per unit mass of oxygen; h_{MT} is the mass transfer coefficient, dependent on the firebrand Sherwood number, particle diameter d_p, and the diffusion coefficient of O_2 in the atmosphere; ρ_{air} is the air density, and YO_2 is the mass fraction of oxygen in the atmosphere. h_{HT} is the heat transfer coefficient, defined by the firebrand Nusselt number, the thermal conductivity of air, and the particle diameter; T_∞ is the ambient air temperature; ε is the effective emissivity of the firebrand (assumed here to be 0.9), and σ is the Stefan–Boltzmann constant. The Sherwood and Nusselt numbers themselves are functions of the Frössling, Schmidt, Prandtl, and particle Reynolds numbers, which can be calculated by assuming some information about particle size, relative velocity, and characteristics of the air like thermal conductivity. The two terms on the right hand of the above equation are the convective and radiative heat fluxes, respectively. Once we have an estimate for temperature as a function of firebrand size and relative velocity, we can use the relation from Anthenien *et al.*,[24] to solve for the rate of change of the firebrand temperature:

$$\frac{dT}{dt} = \frac{-SA}{\rho_p c_p V}\left(h_{HT}(T - T_\infty) + \varepsilon\sigma(T^4 - T_\infty^4)\right), \qquad \text{(B2)}$$

where SA is the surface area of the firebrand, and V is its volume, c_p is the specific heat of the fuel, and ρ_p is its density. We can thus solve for the time it takes a firebrand to cool down from its initial temperature to 798 °C. While this blackbody temperature may not be exact for the specific fuels comprising the firebrands in our experiment, evidence from the color pyrometry experiments of Urban *et al.*[89] does support this assumption, as they observed glowing firebrands ranging from above 750–950 °C.While we lack information about firebrand size for specific trajectories in our recordings, and also lack slip velocity measurements between the buoyant plume and the firebrands, we can solve the system of equations above for a realistic range of slip velocities and the particle sizes we measured in our collection trays. The glowing times for firebrands of various sizes, from 10^{-5} to 10^{-1} m and slip velocities from 0 to 10 ms^{-1} are shown in Fig. 9). Glow time is more sensitive to firebrand size than the relative velocity, though increasing slip velocity does decrease the glowing time by a factor 1.5–5 depending on d_p. We can compare these glow times to the temporal resolution of our camera (119.8 Hz) and our tracking algorithm, which requires particles to be present and tracked for at least three frames before saving. Therefore, any firebrands that cease glowing more quickly than 0.0167 s will not be tracked. This threshold is not far from the glowing time of a 1 mm firebrand, which should glow between 0.04 and 0.08 s according to the above model depending on the relative velocity. This provides additional support to our assumption that we are only tracking the relatively large firebrands in the PTV processing–those greater than 1 mm which mak eup about 3% of all those collected from around the pile over the course of the burn. We observe firebrand trajectories for as long as 1.6 s in our recordings, which would correspond to firebrands on the order of a centimeter according to the above firebrand glowing model. Although the measured trajectory lengths do not correspond to glowing times—as firebrands can be lost in the tracking process due to their out-of-plane motion, or move too fast or too near to other firebrands for the PTV algorithm to reliably track them between frames—it does at least put a lower limit on our size range of firebrand observed in the videos. We are most likely measuring the velocity and accelerations of the largest particles, at a maximum of 3% of firebrands ejected by the pile. Firebrands around 1 cm in size have glow times of 0.5–1 s and comprise only 0.03% of firebrands collected in our trays. However, with over 400 000 firebrands tracked over just the course of the 18-min experiment, such small percentages become significant.

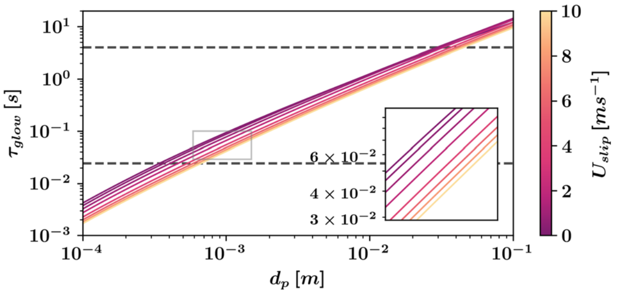

FIG. 9. Estimated time for firebrands of various sizes (and in varying wind conditions as indicated by the different colored lines) to reach 500 °C, the temperature firebrands stop emitting light in the visible spectrum assuming blackbody radiation.

REFERENCES

[1] R. Wadhwani, C. Sullivan, A. Wickramasinghe, M. Kyng, N. Khan, and K. Moinuddin, “A review of firebrand studies on generation and transport,” Fire Safety J. **134**, 103674 (2022).

[2] S. L. Manzello and S. Suzuki, “The world is burning: What exactly are firebrands and why should anyone care?,” Front. Mech. Eng. **8**, 1072214 (2023).

[3] R. Blanchi, A. Maranghides, and J. R. England, in *Encyclopedia of Wildfires and Wildland-Urban Interface (WUI) Fires*, edited by S. L. Manzello (Springer International Publishing, Cham, 2019), pp. 1–14.

[4] M. Kumar, S. Li, P. Nguyen, and T. Banerjee, “Examining the existing definitions of wildland-urban interface for California,” Ecosphere **13**, e4306 (2022).

[5] S. Li, V. Dao, M. Kumar, P. Nguyen, and T. Banerjee, "Mapping the wildland-urban interface in California using remote sensing data," Sci. Rep. **12**, 5789 (2022).

[6] A. Maranghides and W. Mell, "A case study of a community affected by the witch and Guejito Wildland Fires," Fire Technol. **47**, 379 (2011).

[7] F. A. Albini, *Spot Fire Distance from Burning Trees: A Predictive Model*, Vol. 56 (Intermountain Forest and Range Experiment Station, Forest Service, 1979).

[8] C. B. Clements, S. Zhong, S. Goodrick, J. Li, B. E. Potter, X. Bian, W. E. Heilman, J. J. Charney, R. Perna, M. Jang *et al.*, "Observing the dynamics of wildland grass fires: FireFlux—A field validation experiment," Bull. Am. Meteorol. Soc. **88**, 1369 (2007).

[9] C. B. Clements, S. Zhong, X. Bian, W. E. Heilman, and D. W. Byun, "First observations of turbulence generated by grass fires," J. Geophys. Res.: Atmos. **113**, D22, https://doi.org/10.1029/2008JD010014 (2008).

[10] W. E. Heilman, T. Banerjee, C. B. Clements, K. L. Clark, S. Zhong, and X. Bian, "Observations of sweep–ejection dynamics for heat and momentum fluxes during wildland fires in forested and grassland environments," J. Appl. Meteorol. Climatol. **60**, 185 (2021).

[11] A. Desai, W. E. Heilman, N. S. Skowronski, K. L. Clark, M. R. Gallagher, C. B. Clements, and T. Banerjee, "Features of turbulence during wildland fires in forested and grassland environments," Agric. Meteorol. **338**, 109501 (2023).

[12] F. A. Albini, M. E. Alexander, and M. G. Cruz, "A mathematical model for predicting the maximum potential spotting distance from a crown fire," Int. J. Wildland Fires **21**, 609 (2012).

[13] N. Sardoy, J. L. Consalvi, A. Kaiss, A. C. Fernandez-Pello, and B. Porterie, "Numerical study of ground-level distribution of firebrands generated by line fires," Combust. Flame **154**, 478 (2008).

[14] P. L. Andrews, "USDA forest service general," Technical Report INT 194 (1986).

[15] P. L. Andrews, "Current status and future needs of the BehavePlus Fire Modeling System," Int. J. Wildland Fires **23**, 21 (2014).

[16] M. A. Finney, *FARSITE, Fire Area Simulator—Model Development and Evaluation*, Vol. 4 (US Department of Agriculture, Forest Service, Rocky Mountain Research Station, 1998).

[17] C. S. Tarifa, P. P. de Notario, and F. G. Moreno, "On the flight paths and lifetimes of burning particles of wood," Symp. (Int.) Combust. **10**, 1021 (1965).

[18] J. P. Woycheese, P. J. Pagni, and D. Liepmann, "Brand propagation from large-scale fires," in *The Second International Conference of Fire Research and Engineering (ICFRE2)* (Society of Fire Protection Engineers, Boston, MA, 1998), pp. 137–150.

[19] J. P. Woycheese, P. J. Pagni, and D. Liepmann, "Brand propagation from large-scale fires," J. Fire Prot. Eng. **10**, 32 (1999).

[20] E. Koo, "Wildfire models: Firebrands and contiguous spread," Ph.D. thesis (University of California, 2006).

[21] E. Koo, P. Pagni, and R. Linn, "Using FIRETEC to describe firebrand behavior in wildfires," in *10th International Conference on Fire and Materials 2007* (LANL, 2007).

[22] K. Himoto and T. Tanaka, "Transport of disk-shaped firebrands in a turbulent boundary layer," Fire Saf. Sci. **8**, 433 (2005).

[23] N. Sardoy, J.-L. Consalvi, B. Porterie, and A. C. Fernandez-Pello, "Modeling transport and combustion of firebrands from burning trees," Combust. Flame **150**, 151 (2007).

[24] R. A. Anthenien, S. D. Tse, and A. Carlos Fernandez-Pello, "On the trajectories of embers initially elevated or lofted by small scale ground fire plumes in high winds," Fire Saf. J. **41**, 349 (2006).

[25] A. Wickramasinghe, N. Khan, and K. Moinuddin, "Determining firebrand generation rate using physics-based modelling from experimental studies through inverse analysis," Fire **5**, 6 (2022).

[26] C. S. Tarifa, P. Pérez del Notario, F. G. Moreno, and A. R. Villa, *Transport and Combustion of Firebrands* (Instituto Nacional de Tecnica Aeroespacial, Esteban Terradas, Madrid, 1967).

[27] A. G. McArthur, *Fire Behaviour in Eucalypt Forests* (Forestry and Timber Bureau, 1967).

[28] A. J. Petersen, L. Baker, and F. Coletti, "Experimental study of inertial particles clustering and settling in homogeneous turbulence," J. Fluid Mech. **864**, 925 (2019).

[29] L. Brandt and F. Coletti, "Particle-laden turbulence: Progress and perspectives," Annu. Rev. Fluid Mech. **54**, 159 (2022).

[30] R. Wadhwani, D. Sutherland, and K. Moinuddin, in *Proceedings for the 6th International Fire Behavior and Fuels Conference* (International Association of Wildland Fire, 2019).

[31] I. dos Santos and N. Yaghoobian, "Effects of urban boundary layer turbulence on firebrand transport," Fire Saf. J. **135**, 103726 (2023).

[32] I. Santos, B. Mahato, B. Bornhoft, S. Jain, and N. Yaghoobian, "Lagrangian sub-grid-scale modeling applied to evolving firebrand particle transport," in *Center for Turbulence Research Proceedings of the Summer Program 2022* (Stanford University, 2023).

[33] M. Frediani, K. Shamsaei, T. W. Juliano, B. Kosovic, J. Knievel, S. A. Tessendorf, and H. Ebrahimian, "Modeling firebrand spotting in WRF-fire for coupled fire-weather prediction," in *ESS Open Archive*, 15 March 2024.

[34] N. Bouvet, S. S. Wessies, E. D. Link, and S. A. Fink, "A framework to characterize WUI firebrand shower exposure using an integrated approach combining 3D particle tracking and machine learning," Int. J. Multiphase Flow **170**, 104651 (2024).

[35] S. Manzello, A. Maranghides, W. Mell, T. Cleary, and J. Yang, "Firebrand production from burning vegetation," in *International Conference on Forest Fire Research 5th Forest Fire Research* (NIST, Coimbra, 2006).

[36] S. L. Manzello, A. Maranghides, J. R. Shields, W. E. Mell, Y. Hayashi, and D. Nii, "Mass and size distribution of firebrands generated from burning Korean pine (*Pinus koraiensis*) trees," Fire Mater. **33**, 21 (2009).

[37] B. Bahrani, "Characterization of firebrands generated from selected vegetative fuels in wildland fires," Ph.D. thesis (The University of North Carolina at Charlotte, 2020).

[38] T. R. Hudson, R. B. Bray, D. L. Blunck, W. Page, B. Butler, T. R. Hudson, R. B. Bray, D. L. Blunck, W. Page, and B. Butler, "Effects of fuel morphology on ember generation characteristics at the tree scale," Int. J. Wildland Fire **29**, 1042 (2020).

[39] S. Adusumilli, T. Huson, N. Gardner, and D. L. Blunck, "Quantifying production of hot firebrands using a fire-resistant fabric," Int. J. Wildland Fire **30**, 154 (2021).

[40] X. Ju, M. Conkling, M. Hajilou, S. Lin, F. Mostafa, A. Ayyar, A. McDowell, M. Lisano, and M. J. Gollner, "Laboratory quantification of firebrand generation from WUI fuels for model development," Fire Saf. J. **141**, 103921 (2023).

[41] M. Hajilou, S. Hu, T. Roche, P. Garg, and M. J. Gollner, "A methodology for experimental quantification of firebrand generation from WUI fuels," Fire Technol. **57**, 2367 (2021).

[42] X. Ju, M. Lisano, M. Hajilou, P. B. Sunderland, S. I. Stoliarov, L. Yang, and M. J. Gollner, "Quantification of firebrand generation from WUI fuels for model development: Firebrand generation rate, surface temperature and heat release rate," Proc. Combust. Inst. **40**, 105729 (2024).

[43] A. Tohidi and N. B. Kaye, "Stochastic modeling of firebrand shower scenarios," Fire Saf. J. **91**, 91 (2017).

[44] A. Tohidi and N. B. Kaye, "Comprehensive wind tunnel experiments of lofting and downwind transport of non-combusting rod-like model firebrands during firebrand shower scenarios," Fire Saf. J. **90**, 95 (2017).

[45] J. C. Thomas, E. V. Mueller, S. Santamaria, M. Gallagher, M. El Houssami, A. Filkov, K. Clark, N. Skowronski, R. M. Hadden, W. Mell, and A. Simeoni, "Investigation of firebrand generation from an experimental fire: Development of a reliable data collection methodology," Fire Saf. J. **91**, 864 (2017).

[46] J. C. Thomas, E. V. Mueller, M. R. Gallagher, K. L. Clark, N. Skowronski, A. Simeoni, and R. M. Hadden, "Coupled assessment of fire behaviour and firebrand dynamics," Front. Mech. Eng. **7**, 650580 (2021).

[47] Z. Tao, B. Bathras, B. Kwon, B. Biallas, M. J. Gollner, and R. Yang, "Effect of firebrand size and geometry on heating from a smoldering pile under wind," Fire Saf. J. **120**, 103031 (2021).

[48] M. Toloui, S. Riley, J. Hong, K. Howard, L. Chamorro, M. Guala, and J. Tucker, "Measurement of atmospheric boundary layer based on super-large-scale particle image velocimetry using natural snowfall," Exp. Fluids **55**, 1737 (2014).

[49] N. T. Ouellette, H. Xu, and E. Bodenschatz, "A quantitative study of three-dimensional Lagrangian particle tracking algorithms," Exp. Fluids **40**, 301 (2006).

[50] D. A. Khalitov and E. K. Longmire, "Simultaneous two-phase PIV by two-parameter phase discrimination," Exp. Fluids **32**, 252 (2002).

[51] G. A. Voth, A. L. Porta, A. M. Crawford, J. Alexander, and E. Bodenschatz, "Measurement of particle accelerations in fully developed turbulence," J. Fluid Mech. **469**, 121 (2002).

[52] S. Gerashchenko, N. S. Sharp, S. Neuscamman, and Z. Warhaft, "Lagrangian measurements of inertial particle accelerations in a turbulent boundary layer," J. Fluid Mech. **617**, 225 (2008).

[53] A. Nemes, T. Dasari, J. Hong, M. Guala, and F. Coletti, "Snowflakes in the atmospheric surface layer: Observation of particle–turbulence dynamics," J. Fluid Mech. **814**, 592 (2017).

[54] M. Ebrahimian, R. S. Sanders, and S. Ghaemi, "Dynamics and wall collision of inertial particles in a solid–liquid turbulent channel flow," J. Fluid Mech. **881**, 872 (2019).

[55] T. Berk and F. Coletti, "Dynamics of small heavy particles in homogeneous turbulence: A Lagrangian experimental study," J. Fluid Mech. **917**, A47 (2021).

[56] R. M. Echols, "Uniformity of wood density assessed from X-rays of increment cores," Wood Sci. Technol. **7**, 34 (1973).

[57] L. A. Bouffier, B. L. Gartner, and J.-C. Domec, "Wood density and hydraulic properties of ponderosa pine from the Willamette valley vs. the Cascade Mountains," Wood Fiber Sci. **35**, 217 (2003). https://wfs.swst.org/index.php/wfs/article/view/1750

[58] N. L. Osborne, Ø. A. Høibø, and D. A. Maguire, "Estimating the density of coast Douglas-fir wood samples at different moisture contents using medical X-ray computed tomography," Comput. Electron. Agric. **127**, 50 (2016).

[59] V. N. Egorova, A. Trucchia, and G. Pagnini, "Fire-spotting generated fires. Part II: The role of flame geometry and slope," Appl. Math. Modell. **104**, 1 (2022).

[60] J. P. Woycheese, "Brand lofting and propagation from large-scale fires," Ph.D. thesis (University of California, 2000).

[61] H.-H. Wang, "Analysis on downwind distribution of firebrands sourced from a wildland fire," Fire Technol. **47**, 321 (2011).

[62] W. Thurston, J. D. Kepert, K. J. Tory, R. J. B. Fawcett, W. Thurston, J. D. Kepert, K. J. Tory, and R. J. B. Fawcett, "The contribution of turbulent plume dynamics to long-range spotting," Int. J. Wildland Fire **26**, 317 (2017).

[63] J. Martin and T. Hillen, "The spotting distribution of wildfires," Appl. Sci. **6**, 177 (2016).

[64] S. L. Manzello, J. R. Shields, T. G. Cleary, A. Maranghides, W. E. Mell, J. C. Yang, Y. Hayashi, D. Nii, and T. Kurita, "On the development and characterization of a firebrand generator," Fire Saf. J. **43**, 258 (2008).

[65] M. El Houssami, E. Mueller, A. Filkov, J. C. Thomas, N. Skowronski, M. R. Gallagher, K. Clark, R. Kremens, and A. Simeoni, "Experimental procedures characterising firebrand generation in wildland fires," Fire Technol. **52**, 731 (2016).

[66] A. Tohidi, N. Kaye, and W. Bridges, "Statistical description of firebrand size and shape distribution from coniferous trees for use in Metropolis Monte Carlo simulations of firebrand flight distance," Fire Saf. J. **77**, 21 (2015).

[67] A. Filkov, S. Prohanov, E. Mueller, D. Kasymov, P. Martynov, M. E. Houssami, J. Thomas, N. Skowronski, B. Butler, M. Gallagher, K. Clark, W. Mell, R. Kremens, R. M. Hadden, and A. Simeoni, "Investigation of firebrand production during prescribed fires conducted in a pine forest," Proc. Combust. Inst. **36**, 3263 (2017).

[68] J. F. Kok, "A scaling theory for the size distribution of emitted dust aerosols suggests climate models underestimate the size of the global dust cycle," Proc. Nat. Acad. Sci. **108**, 1016 (2011).

[69] Y. Chen and H. Sundaram, in *2005 IEEE 7th Workshop on Multimedia Signal Processing* (IEEE, 2005), pp. 1–4.

[70] S. Xiao, Y. Cui, J. Brahney, N. M. Mahowald, and Q. Li, "Long-distance atmospheric transport of microplastic fibres influenced by their shapes," Nat. Geosci. **16**, 863 (2023).

[71] G. Heskestad, "Engineering relations for fire plumes," Fire Saf. J. **7**(1), 25–32 (1984).

[72] W. Mell, A. Maranghides, R. McDermott, and S. L. Manzello, "Numerical simulation and experiments of burning Douglas fir trees," Combust. Flame **156**, 2023 (2009).

[73] A. M. Obukhov, "The structure of the temperature field in a turbulent flow," Izv. Akad. Nauk. SSSR Ser. Geogr. Geofiz. **13**, 58 (1949).

[74] S. Corrsin, "On the spectrum of isotropic temperature fluctuations in an isotropic turbulence," J. Appl. Phys. **22**, 469 (1951).

[75] G. Katul, A. Porporato, D. Cava, and M. Siqueira, "An analysis of intermittency, scaling, and surface renewal in atmospheric surface layer turbulence," Phys. D: Nonlinear Phenom. **215**, 117 (2006).

[76] S. Chowdhuri, K. Ghannam, and T. Banerjee, "A scale-wise analysis of intermittent momentum transport in dense canopy flows," J. Fluid Mech. **942**, A51 (2022).

[77] S. Chowdhuri, T. Kalmár-Nagy, and T. Banerjee, "Persistence analysis of velocity and temperature fluctuations in convective surface layer turbulence," Phys. Fluids **32**, 076601 (2020).

[78] S. E. Caton-Kerr, A. Tohidi, and M. J. Gollner, "Firebrand generation from thermally-degraded cylindrical wooden dowels," Front. Mech. Eng. **5**, 32 (2019).

[79] G. J. McCarthy, K. G. Tolhurst, and K. Chatto, *Overall Fuel Hazard Guide* (Fire Management, Department of Natural Resources & Environment, 1999).

[80] S. Ayyalasomayajula, A. Gylfason, L. R. Collins, E. Bodenschatz, and Z. Warhaft, "Lagrangian measurements of inertial particle accelerations in grid generated wind tunnel turbulence," Phys. Rev. Lett. **97**, 144507 (2006).

[81] H. Parishani, O. Ayala, B. Rosa, L.-P. Wang, and W. W. Grabowski, "Effects of gravity on the acceleration and pair statistics of inertial particles in homogeneous isotropic turbulence," Phys. Fluids **27**, 033304 (2015).

[82] J. Bec, L. Biferale, M. Cencini, A. Lanotte, S. Musacchio, and F. Toschi, "Heavy particle concentration in turbulence at dissipative and inertial scales," Phys. Rev. Lett. **98**, 084502 (2007).

[83] H. Baum and B. Mccaffrey, "Fire induced flow field—Theory and experiment," Fire Saf. Sci. **2**, 129 (1989).

[84] S. Tse and A. Fernandez-Pello, "On the flight paths of metal particles and embers generated by power lines in high winds—a potential source of wildland fires," Fire Saf. J. **30**, 333 (1998).

[85] H. Huang, R. Ooka, S. Kato, H. Otake, and Y. Hayashi, "CFD simulation of thermal plume and firebrands scattering in urban fire," Fire Sci. Technol. **23**, 152 (2004).

[86] A. Tinklenberg, M. Guala, and F. Coletti, "Thin disks falling in air," J. Fluid Mech. **962**, A3 (2023).

[87] J. D. Kepert, W. Thurston, and K. J. Tory, "A fast, physically based model of firebrand transport by bushfire plumes," Agric. Meteorol. **345**, 109839 (2024).

[88] E. S. Baker, "Burning characteristics of individual Douglas-fir trees in the wildland/urban interface," Ph.D. thesis (Worcester Polytechnic Institute, 2011).

[89] J. L. Urban, M. Vicariotto, D. Dunn-Rankin, and A. C. Fernandez-Pello, "Temperature measurement of glowing embers with color pyrometry," Fire Technol. **55**, 1013 (2019).

[90] R. R. Linn, J. M. Reisner, J. J. Colman, and J. L. Winterkamp, "Studying wildfire behavior using FIRETEC," Int. J. Wildland Fire **11**(3–4), 233–246 (2002).